



HAL
open science

Tajik Basin and Southwestern Tian Shan, Northwestern India-Asia Collision Zone: 2. Timing of Basin Inversion, Tian Shan Mountain Building, and Relation to Pamir-Plateau Advance and Deep India-Asia Indentation

Sanaa Abdulhameed, Lothar Ratschbacher, Raymond Jonckheere, Łukasz Gałala, Eva Enkelmann, Alexandra Kässner, Myriam Kars, Adam Szulc, Sofia-Katerina Kufner, Bernd Schurr, et al.

► To cite this version:

Sanaa Abdulhameed, Lothar Ratschbacher, Raymond Jonckheere, Łukasz Gałala, Eva Enkelmann, et al.. Tajik Basin and Southwestern Tian Shan, Northwestern India-Asia Collision Zone: 2. Timing of Basin Inversion, Tian Shan Mountain Building, and Relation to Pamir-Plateau Advance and Deep India-Asia Indentation. *Tectonics*, 2020, 39 (5), pp.e2019TC005873. 10.1029/2019TC005873 . insu-02873590

HAL Id: insu-02873590

<https://insu.hal.science/insu-02873590>

Submitted on 18 Jun 2020

HAL is a multi-disciplinary open access archive for the deposit and dissemination of scientific research documents, whether they are published or not. The documents may come from teaching and research institutions in France or abroad, or from public or private research centers.

L'archive ouverte pluridisciplinaire **HAL**, est destinée au dépôt et à la diffusion de documents scientifiques de niveau recherche, publiés ou non, émanant des établissements d'enseignement et de recherche français ou étrangers, des laboratoires publics ou privés.

Tectonics

RESEARCH ARTICLE

10.1029/2019TC005873

This article is a companion to Dedow et al. (2020) <https://doi.org/10.1029/2019TC005874>, Gagala et al. (2020) <https://doi.org/10.1029/2019TC005871>.

Key Points:

- ~40- to 15-Ma sediment loading reheated the southern Tian Shan; major Tajik-basin inversion and Tian Shan mountain building started at ~12 Ma
- ~12-Ma shortening immediately spread to foreland buttresses and external fold-thrust belt; reactivation affected its interior
- Tajik-basin inversion and major Tian Shan mountain building were induced by lithospheric indentation of India into Asia beneath the Pamir

Supporting Information:

- Supporting Information S1
- Table S1
- Table S2
- Table S3
- Table S4
- Figure S1
- Figure S2
- Figure S3
- Figure S4

Correspondence to:

S. Abdulhameed and L. Ratschbacher, lothar@geo.tu-freiberg.de; sanaa.a.hameed@gmail.com

Citation:

Abdulhameed, S., Ratschbacher, L., Jonckheere, R., Gagala, L., Enkelmann, E., Käbner, A., et al. (2020). Tajik basin and southwestern Tian Shan, northwestern India-Asia collision zone: 2. Timing of basin inversion, Tian Shan mountain building, and relation to Pamir-plateau advance and deep India-Asia indentation. *Tectonics*, 39, e2019TC005873. <https://doi.org/10.1029/2019TC005873>

Received 3 SEP 2019

Accepted 14 MAR 2020

Accepted article online 18 MAR 2020

Corrected 20 MAY 2020

This article was corrected on 20 MAY 2020. See the end of the full text for details.

©2020. American Geophysical Union. All Rights Reserved.

Tajik Basin and Southwestern Tian Shan, Northwestern India-Asia Collision Zone: 2. Timing of Basin Inversion, Tian Shan Mountain Building, and Relation to Pamir-Plateau Advance and Deep India-Asia Indentation

Sanaa Abdulhameed¹ , Lothar Ratschbacher¹ , Raymond Jonckheere¹ , Lukasz Gagala^{1,2} , Eva Enkelmann³ , Alexandra Käbner¹ , Myriam A. C. Kars⁴ , Adam Szulc^{1,5} , Sofia-Katerina Kufner⁶ , Bernd Schurr⁶ , Jean-Claude Ringenbach⁷, Mykhaylo Nakapelyukh^{1,8}, Jahanzeb Khan^{1,9} , Mustafo Gadoev¹⁰ , and Ilhomjon Oimahmadov¹⁰

¹Geologie, Technische Universität Bergakademie Freiberg, Freiberg, Germany, ²Now at Hellenic Petroleum, Marousi, Greece, ³Department of Geoscience, University of Calgary, Calgary, Alberta, Canada, ⁴Center for Advanced Marine Core Research, Kochi University, Nankoku, Japan, ⁵Now at CASP, Cambridge, UK, ⁶Deutsches GeoForschungsZentrum GFZ, Potsdam, Germany, ⁷E2S-UPPA, CNRS, University Pau and Pays Adour, Pau, France, ⁸Now at S. I. Subbotin Institute of Geophysics, NAS, Kyiv, Ukraine, ⁹Now at Institute of Geology, The University of Azad Jammu and Kashmir, Muzaffarabad, Pakistan, ¹⁰Institute of Geology, Earthquake Engineering and Seismology, Tajik Academy of Sciences, Dushanbe, Tajikistan

Abstract The Tajik basin and southwestern Tian Shan constitute the northwestern tip of the India-Asia collision zone. Basin inversion formed the thin-skinned Tajik fold-thrust belt, outlined by westward convex fold trains, underlain by a décollement in Jurassic evaporites. The belt's leading edge—the Uzbek Gissar—and its transpressional northern lateral margin—the Tajik Gissar—constitute the thick-skinned foreland buttresses. Apatite fission-track data indicate ~40- to 15-Ma reheating by sediment burial in the Tian Shan. In the Gissar and the Tajik fold-thrust belt, apatite fission-track and (U,Th)/He ages date the major phase of shortening/erosion between ~12 and 1 Ma, with exhumation to 2- to 3-km crustal depths within a few Myr after onset of shortening. Shortening spread immediately across the fold-thrust belt, typical for belts floored by a detachment in ductile rocks, and into the foreland buttresses. Reactivation concentrated in the internal (eastern) fold-thrust belt with the thickest evaporates. The youngest ages (~6.6–1.6 Ma) occur along the Vakhsh thrust, the active erosional front of the fold-thrust belt in the northeastern Tajik basin, where it narrows between the converging Tian Shan and Pamir. Our study links major events in the Pamir hinterland with the Tajik basin and Tian Shan foreland. In the late Eocene–early Miocene, the advancing Pamir-plateau crust loaded the foreland, inducing subsidence, reheating, and early shortening. Basin inversion and major shortening/transpression in the foreland buttresses from ~12 Ma onward were synchronous with the subcrustal indentation of Indian lithosphere into the Tajik-Tarim basin lithosphere and the onset of its rollback beneath the Pamir.

1. Introduction

The Tajik basin of Central Asia is a retro-foreland basin with ~7–10 km, southward and eastward thickening, Mesozoic-Cenozoic strata at the northwestern tip of the India-Asia collision zone (Figure 1a; e.g., Burtman & Molnar, 1993; Carrapa et al., 2015; Chapman et al., 2019; Klocke et al., 2017; Nikolaev, 2002). Jurassic-Oligocene pre-tectonic, shallow-marine to continental strata evolved into Neogene synorogenic, continental clastic deposits derived from the Tian Shan in the north and the Pamir and Hindu Kush in the east and south. Inversion of the basin into the Tajik fold-thrust belt (FTB) occurred during the Neogene, but the structural evolution, timing, and relationship to the Pamir and Tian Shan are under discussion (e.g., Bourgeois et al., 1997; Chapman et al., 2017; Stübner, Ratschbacher, Rutte, et al., 2013; Jepson, Glorie, Konopelko, Gillespie, et al., 2018; Käbner et al., 2016; Kufner et al., 2018; Schneider et al., 2019; Schurr et al., 2014; Thomas, Chauvon, et al., 1994).

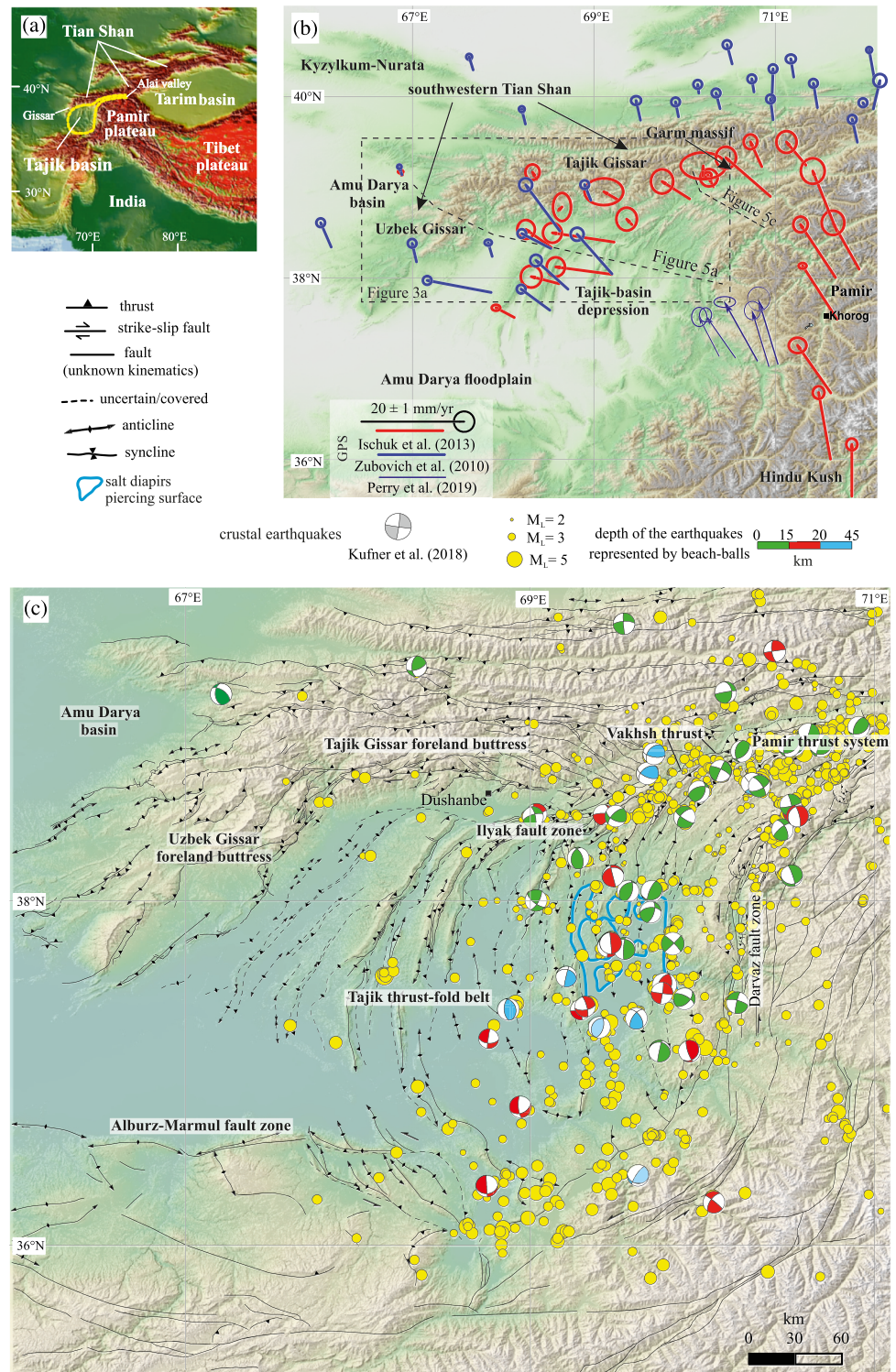


Figure 1. Active tectonics of the Tajik basin and surrounding mountain ranges. (a) Location of the Tajik basin at the western tip of the India-Asia collision zone. (b) Digital elevation model with GNSS velocity vectors. (c) New fold-fault map of Cenozoic structures of the Tajik basin and surrounding thick-skinned fold-thrust belts. Interpreted from 1:200,000 geological maps and Soviet seismic and drill-hole data (compilation in Gaglia et al., 2020), the Geological and Mineral Resource Map of Afghanistan (Doeblich & Wahl, 2006), satellite images (Google Earth®), and fieldwork between 2004 and 2014.

As indicated by the present deformation field measured by Global Navigation Satellite System (GNSS; e.g., Ischuk et al., 2013; Perry et al., 2019; Zubovich et al., 2010, 2016), the Pamir moves north relative to stable Asia with little internal seismic deformation in its eastern part (Schurr et al., 2014). The western Pamir shows higher seismic deformation rates, expressed by strike-slip and normal faults, indicating ~E-W extension together with ~N-S shortening. The Pamir's northern margin thrusts over the intramontane Alai valley—remnant of a once contiguous Tajik-Tarim basin system—causing intense seismicity along the Pamir thrust system (Figures 1b and 1c; Schurr et al., 2014; Sippl et al., 2014). Schurr et al. (2014) and Kufner et al. (2018) explained the active deformation field by a combination of bulk northward displacement (Pamir orocline growth) and synchronous collapse and westward lateral material flow (“lateral extrusion,” cf. Ratschbacher et al., 1991) of the Pamir plateau (~4 km average elevation) into the Tajik-basin depression (~1 km average elevation); there, extrusion causes thin-skinned, ~NW-SE shortening of the Tajik-basin strata above an evaporitic décollement and thick-skinned shortening along the frontal and lateral foreland buttresses (Figure 1c). The northward movement and westward extrusion combine to cause the progressive rotation of the GNSS surface velocities from ~NNW to ~WNW from the eastern Pamir to the Tajik basin (Figure 1b).

Intense intermediate-depth (~70–300 km) seismicity attests to subcrustal processes in the Hindu Kush and the Pamir (e.g., Kufner et al., 2017, 2016; Mechie et al., 2012; Pegler & Das, 1998; Schneider et al., 2013, 2019; Sippl, Schurr, Tympel, et al., 2013; Sippl, Schurr, Yuan, et al., 2013). Beneath the Hindu Kush, subduction of marginal Indian continental crust was inferred. Underneath the Pamir, the seismicity outlines an arcuate slab (“Pamir slab”), dipping ~E beneath the western and ~S beneath the eastern Pamir; it likely traces delamination and rollback of Asian (Tajik-Tarim) lower crust and mantle beneath thickened (65–75 km) Pamir crust. Kufner et al. (2016) inferred that the northward advancing cratonic Indian lithosphere is forcing the delamination and rollback of Asian lithosphere (basement of the Tajik-Tarim basins). They calculated that the delamination of ~380 km of Asian lithosphere at ~34 mm/year—the India-Asia convergence rate in the western collision zone (Molnar & Stock, 2009)—has taken ~12–11 Myr.

Along the western deformation front of the India-Asia collision, the Pamir interacts with the Tian Shan (Figure 1). Käßner et al. (2016) showed, based on apatite fission-track (AFT) and (U,Th)/He (AHe) thermochronology, that moderate reheating in the southwestern Tian Shan (Tajik Gissar, including the Garm massif; Figure 1b) occurred between ~40 and 15 Ma; accelerated exhumation/cooling took place over the last ~10 Myr. High exhumation rates correlate with pronounced local relief, produced by Cenozoic faults reactivating upper Paleozoic structures, and inversion of Mesozoic-Cenozoic intra-montane basins. Structurally, the Tajik Gissar is a broad, ~E trending zone of dextral transpression that includes the northern Tajik basin (Ilyak fault zone; Leith & Simpson, 1986) and the Pamir thrust system of the Pamir's northern margin (Figure 1c). It is the active deformation field described above (Kufner et al., 2018; Schurr et al., 2014)—the interaction of the westward collapse of the Pamir plateau into the Tajik-basin depression with the bulk northward motion of the Pamir—that transformed the southwestern Tian Shan into a dextral transpressional belt.

Figure 2a provides a sketch of the—above described—neotectonic deformation of the Pamir and the Tian Shan foreland adopted from Schurr et al. (2014), Käßner et al. (2016), and Kufner et al. (2018). It shows Indian lithosphere at subcrustal depths with the orange lines marking the outline of the transfer corridors between the underthrusting cratonic India under the Pamir and the subducting marginal Indian crust in the Hindu Kush (cf. Kufner et al., 2018, 2016). The green arrows show the directions of material flow within the crust imposed by the Indian convergence at depth. The yellow band outlines the current position of the leading edge of subcrustal cratonic India at the surface. The red arrows show the material flow directions in the Pamir upper-middle crust. The red stippled lines and arrows in the center of the diagram trace the principal active fault pattern of the western Pamir and the associated deformation field. The beach balls show representative focal-mechanism solutions for the active deformation field. Figure 2b sketches the constraints imposed by the foreland shortening of the Asian (Tajik) crust on the geometry of the Tajik-basin lithosphere (Pamir slab) beneath the Pamir (cf. Gągała et al., 2020). Sippl, Schurr, Yuan, et al., 2013) interpreted the subvertical cluster of seismicity between ~100- and 200-km depth as representing eclogitized Asian (Tajik) lower crust, overlain between 60 and 100 km by subducted middle crust. Thus, the seismicity cluster and the subducted Tajik middle crust approximate the down-dip extension of the detachment(s) of the Tajik FTB and its basement. This geometry defines the curved upper interface of the rolling back Tajik-basin lithosphere and is mimicked by the Tajik Moho down to ~90 km (Schneider et al., 2019). The ≥ 175 -km shortening estimates in

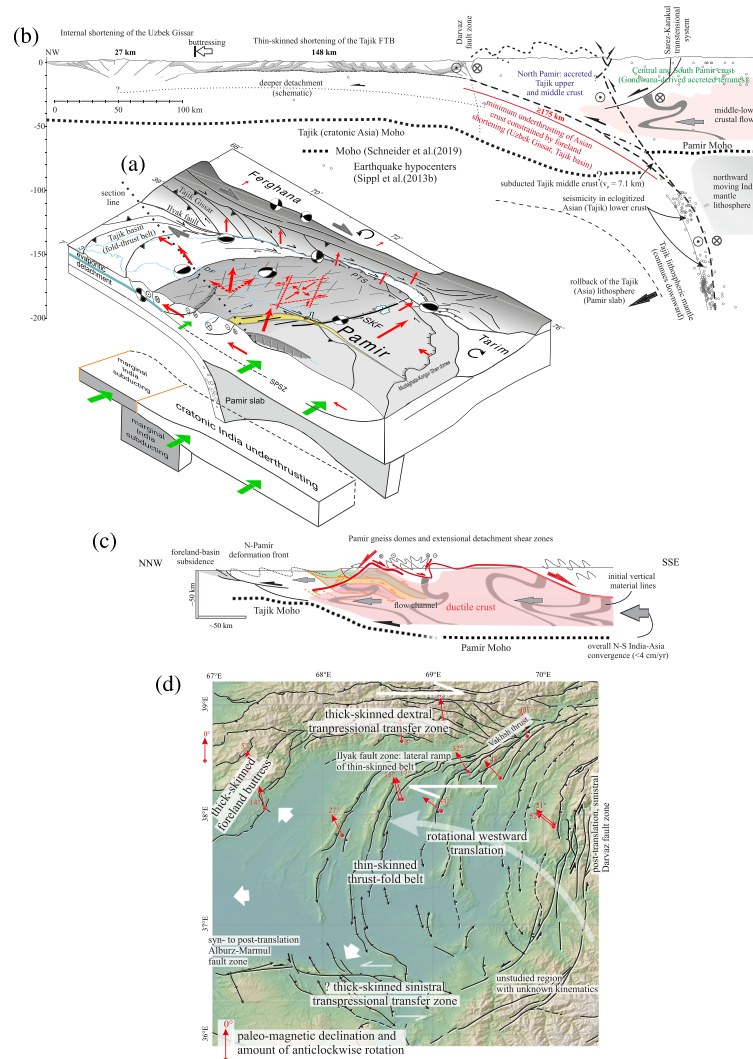


Figure 2. (a) Diagram, modified from Schurr et al. (2014), Käbner et al. (2016), and Kufner et al. (2018), sketching the neotectonics of the Pamir, Tajik basin, and the southwestern Tian Shan, and its driver, the Indian lithosphere at subcrustal depths (crustal and lithospheric thickness not to scale). The orange lines in the subcrustal lithosphere mark the outline of the transfer corridors separating subducting marginal India from underthrusting cratonic India. The green arrows show directions of material flow imposed by the India-Asia convergence. The yellow band outlines the current position of the leading edge of the cratonic India at depth projected onto the surface. The red arrows show material flow directions in the upper crust. The stippled lines and arrows in the center of the diagram trace principal fault pattern of the western Pamir. The beach balls show representative focal-mechanism solutions for the active deformation field. The Pamir is pushed northward, with shortening concentrated along its northern perimeter, the Pamir thrust system (PTS). At the same time, the Pamir deforms internally by strike-slip and normal faulting, producing ~E-W extension, causing westward extrusion under overall N-S shortening. The westward flow imposes shortening of the Tajik-basin sedimentary rocks above an evaporitic décollement. The northern transfer zone of the westward flow zone is accommodated along a broad dextral transpression corridor, comprising the Pamir thrust system, the Ilyak fault, and the Gissar range of the southwestern Tian Shan. SKF = Sarez-Karakul fault system. (b) Cross-sectional sketch of the constraints imposed by the foreland shortening of the Asian (Tajik) crust on the geometry of the Tajik-basin lithosphere (Pamir slab) beneath the Pamir (cf. Gagala et al., 2020). The seismicity cluster and subducted Tajik middle crust approximate the down-dip extension of the detachment(s) of the Tajik fold-thrust belt and its basement. This geometry defines the curved upper interface of the rolling back Tajik-basin lithosphere and is mimicked by the Tajik Moho. The shortening estimates in the Tian Shan (Uzbek Gissar) and the Tajik fold-thrust belt and the yet unquantified amounts of accretion and deep subduction of Tajik (Asian) upper and middle crust in and beneath the North Pamir are considered a proxy for the amount of convergence since ~12 Ma. The sinistral-normal Karakul-Sarez fault system and the red zone on the right side of the cross section highlight the upper to lower crustal flow from the Pamir-plateau crust to the foreland. (c) Cross-sectional sketch of the ~23- to 15-Ma evolution of the Pamir and its foreland. The ~37- to 20-Ma crustal thickening is sketched by the thrust stacks and recumbent fold nappes of the Central Pamir. Gravitational collapse of the Pamir-plateau crust followed, including the normal-sense shear zone of the Central and southwestern Pamir. The collapse of the leading edge of the Pamir plateau transferred the deformation from the Central to the North Pamir. The ductile crust (red) is dragging the middle and upper crust foreland-ward. The model geometries and kinematics are akin to models proposed for foreland-directed plateau collapse (Rey et al., 2010). (d) Major structural features of the Tajik fold-thrust belt and surrounding mountain ranges (Tian Shan in the north, Pamir on the right). Pamir orocline northward and westward advance and synchronous westward upper crustal flow induce structural asymmetry with much larger dextral strike-slip along the northern margin of the fold-thrust belt than sinistral strike-slip along its southern margin. See text for references and discussion.

the Tian Shan foreland and the Tajik FTB (Gagała et al., 2020) and the yet unquantified amounts of accretion and deep subduction (Sippl, Schurr, Yuan, et al., 2013) of Tajik (Asian) upper and middle crust in and beneath the North Pamir are considered a proxy for the amount of convergence since ~12 Ma. The deep-reaching seismic zone in this scenario constitutes an incomplete Tajik lithosphere, deprived of its middle and upper crustal layer, the middle crust partly subducted to 80–100 km, and—together with the upper crust—accreted to the hanging-wall and forming the North Pamir and the Tajik FTB. The sinistral-normal Karakul-Sarez fault system and the red zone on the right side of the cross section sketch the upper to lower crustal flow from the thick Pamir-plateau crust to the foreland depression (Sass et al., 2014; Stübner, Ratschbacher, Rutte, et al., 2013).

The ~20- to 12-Ma evolution of the Pamir is characterized by the northward advance and simultaneous foreland-directed gravitational collapse of the Pamir plateau (Hacker et al., 2017; Robinson et al., 2004, 2007; Rutte, Ratschbacher, Khan, et al., 2017; Rutte, Ratschbacher, Schneider, et al., 2017; Stübner, Ratschbacher, Rutte, et al., 2013; Stübner, Ratschbacher, Weise, et al., 2013; Schurr et al., 2014; Worthington et al., 2020). The foreland advance has been accommodated by bulk foreland propagation of the Pamir orocline and coeval synconvergent crustal extension in the Pamir, in particular in the gneiss domes of the Pamir plateau. Following intense Paleogene crustal thickening, the domes of the Central and East Pamir (Yazgulom-Sarez-Muskol-Shatput-Muztaghata) were exhumed under ~N-S extension along normal-sense shear zones between ~20–15 Ma and—under decreasing rates—~12 Ma, when shortening resumed. The ~N-S extension in the South Pamir gneiss domes (Shakh dara-Alichur) was active longer (~6–2 Ma). About E–W extension is active along the Kongur Shan extensional detachment of the East Pamir and the sinistral-normal Sarez-Karakul fault system that transects the Pamir NNE-SSW (Figure 2a). The switch from crustal shortening to upper to (partly) lower crustal extension throughout the Pamir and Hindu Kush at ~23–20 Ma was contemporaneous with the proposed slab breakoff of Greater India from Cratonic India, which likely resulted in an elevated gravitational potential in the Pamir, triggering crustal collapse (e.g., Replumaz et al., 2010; Stearns et al., 2013, 2015; Rutte, Ratschbacher, Khan, et al., 2017; Rutte, Ratschbacher, Schneider, et al., 2017). Figure 2c sketches the ~20- to 12-Ma evolution by a hinterland (Pamir plateau) to foreland (North Pamir and Tajik basin) cross section. The ~37- to 20-Ma crustal thickening—diagrammatically shown by the thrust stacks and recumbent fold nappes of the Central Pamir—was followed by gravitational collapse of the Pamir plateau, including the top-to-~N, normal-sense shear zone of the Central Pamir and the top-to-~SSE, normal-sense detachment zone of the southwestern Pamir. The ~20-Ma onset of collapse of the leading edge of the Pamir plateau in the Central Pamir is interpreted to drive shortening north and northwest of it, transferring the deformation from the Central to the North Pamir (Rutte, Ratschbacher, Khan, et al., 2017; Rutte, Ratschbacher, Schneider, et al., 2017; Stübner, Ratschbacher, Rutte, et al., 2013; Stübner, Ratschbacher, Weise, et al., 2013; Worthington et al., 2020). The ductile crust (red in Figure 2c) is dragging the middle and upper crust foreland-ward, mimicking the current displacement field, however—given the at this time still large distance to the foreland buttresses—the flow was mostly northward. The model geometries and kinematics are akin to models proposed for foreland-directed plateau collapse, modeled, for example, by Rey et al. (2010), their Figures 2 and 3).

Herein, our major goal is to extend the “northward indentation-westward flow” tectonic model of the active deformation field (Figures 2a and 2b) in time and investigate the onset and progression of the inversion of the Tajik basin, and the age of the involvement of the western (Uzbek Gissar) and northern (Tajik Gissar) foreland buttresses of the Tajik FTB in the southwestern Tian Shan (Figure 1c). In part 1 of this paper series, Gagała et al. (2020) detail the structures, kinematics, and amount of shortening during the evolution of the Tajik FTB and its foreland; in part 3, Dedow et al. (2020) specify the preorogenic and synorogenic tectono-sedimentary evolution of the eastern Tajik basin. Here, we provide estimates of burial temperatures from vitrinite-reflectance maturity data of the Jurassic to Upper Cretaceous (Cr₂) strata of the Tajik basin and the Uzbek and Tajik Gissar, and zircon (U,Th)/He (ZHe), AFT, and AHe thermochronologic dates from samples of crystalline basement rocks of the Tajik and Uzbek Gissar, and the Jurassic to Lower Cretaceous (Cr₁) clastic rocks of the Tajik basin, exhumed along the thrusts of the Tajik FTB. We show that inversion of the Tajik basin and shortening in the Gissar commenced at ~12 Ma; seismicity and geodesy demonstrate that it is ongoing. Finally, we link the two major tectonic events in the Pamir hinterland, Tajik basin, and Tian Shan foreland, suggesting that the Paleogene-early Miocene thickened, northward advancing, and collapsing Pamir-plateau crust loaded the foreland, causing burial, moderate reheating, and local exhumation at

~40–15 Ma. The coupling between the subcrustal Indian and Asian (Tajik-Tarim) lithospheres initiated the Tajik-basin inversion and started the major phase of Cenozoic Tian Shan mountain building at ~12 Ma.

2. Structural and Stratigraphic Framework of the Tajik Basin and the Southwestern Tian Shan

Internally, the Tajik basin features ~N-NE trending valleys and ridges (Figures 1b and 1c); they comprise buried synclinoria and eroded anticlinoria (e.g., Thomas, Chauvin, et al., 1994; Nikolaev, 2002; Gaġala et al., 2020). Toward the north, the thrusts and folds of the Tajik FTB bend ~E and merge with the dextral transpressive Ilyak fault zone, a basement-rooted lateral ramp, in the northern Tajik basin (Gaġala et al., 2020; Kufner et al., 2018). To the south in Afghanistan, the ~E trending Alburz-Marmul fault, an active dextral fault zone (e.g., Ruleman et al., 2007), cuts ~NW trending folds and thrusts that connect—mostly concealed by the Amu-Darya River floodplain—with those of the central Tajik basin. The Tajik FTB is detached along evaporites, the Late Jurassic Gaurdak Formation (e.g., Bekker, 1996; Burtman, 2000; Nikolaev, 2002).

Figure 2d summarizes the key structures and kinematics of the Tajik FTB and its foreland buttresses (Babaev, 1975; Bourgeois et al., 1997; Käßner et al., 2016; Gaġala et al., 2020; Thomas, Chauvin, et al., 1994; Thomas, Gapais, et al., 1994; Thomas et al., 1996). The Uzbek Gissar—a basement culmination—forms the frontal foreland buttress of the Tajik FTB; it overrides the western margin of the Tajik basin and the eastern margin of the Amu-Darya basin along ~200-km-long, thick-skinned thrust fronts, forming an asymmetric pop-up structure (Figure 1c). In the northeast, the basement-cored thrust imbricates of the Uzbek Gissar connect to a broad belt of dextral transpression with a northward diminishing strike-slip component in the southwestern Tian Shan—the Tajik Gissar. In the south, they plunge SW and disappear beneath the Amu-Darya floodplain. Thus, the Ilyak fault zone and the broad belt of dextral transpression in the southwestern Tian Shan and the en-échélon folds and thrusts south of the Amu-Darya floodplain constitute the northern dextral and southern sinistral oblique-lateral ramps of the westward advancing Tajik FTB, respectively. Paleomagnetic data indicate 0–53° anticlockwise rotations in the northern Tajik basin (Abdullaev & Rzhovsky, 1973; Bazhenov et al., 1994; Pozzi & Feinberg, 1991; Thomas, Chauvin, et al., 1994); this suggests much greater dextral shear along the Tajik FTB northern margin than sinistral shear along its southern margin.

The Gissar and the Tajik basin feature an ~7- to 10-km thick sedimentary sequence (Figure S1 in the supporting information). The full basal section crops out only in the Uzbek and Tajik Gissar, where local Triassic and widespread Lower Jurassic strata onlap the crystalline basement (Figure 3a). The décollement along the Upper Jurassic evaporites defines the base of the known section in the Tajik basin. The preorogenic strata comprise Lower-Middle Jurassic coal-bearing clastic rocks followed by shallow-marine limestones, Upper Jurassic evaporites, Lower Cretaceous (Cr₁) red beds, and variegated Upper Cretaceous (Cr₂) to Oligocene shallow-marine strata. Upper Oligocene-Miocene to Recent, synorogenic, mostly coarse-grained clastic rocks comprise more than half (4–9 km) of the sedimentary section (e.g., GRI, 1961–1964; see Text S1 in the supporting information; Carrapa et al., 2015; Chapman et al., 2019; Klocke et al., 2017; Vlasov et al., 1991).

3. Samples and Methods

We analyzed vitrinite reflectance (Ro) in organic-rich samples from Lower-Middle Jurassic, Cr₁, and Cr₂ strata to determine thermal maturity; the analyzed lithologies comprised black shale, marl, and coal and represent kerogen types II/III. The samples were analyzed at TOTAL, Pau, France, and TU Bergakademie Freiberg, Germany, following standard procedures (Taylor et al., 1998). Table S1 in the supporting information lists the samples and provides the total organic carbon, and Ro (in %). We converted the %Ro values into burial temperatures following Barker and Goldstein (1990) and Sweeney and Burnham (1990). The first developed an empirical relationship derived from a large dataset; the latter established an experimentally derived kinetic model. The temperatures obtained from these two approaches differ by up to 30 °C: The Sweeney and Burnham (1990) estimates yield higher values than those of Barker and Goldstein (1990) for temperatures less than ~130 °C, and the relationship is reverse for temperatures higher than ~130 °C; around 130 °C the values are identical.

We used AFT and AHe thermochronology for the timing of displacement and erosion along the intrabasin thrust-cored anticlines and the basement-involving ranges of the southwestern Tian Shan. These

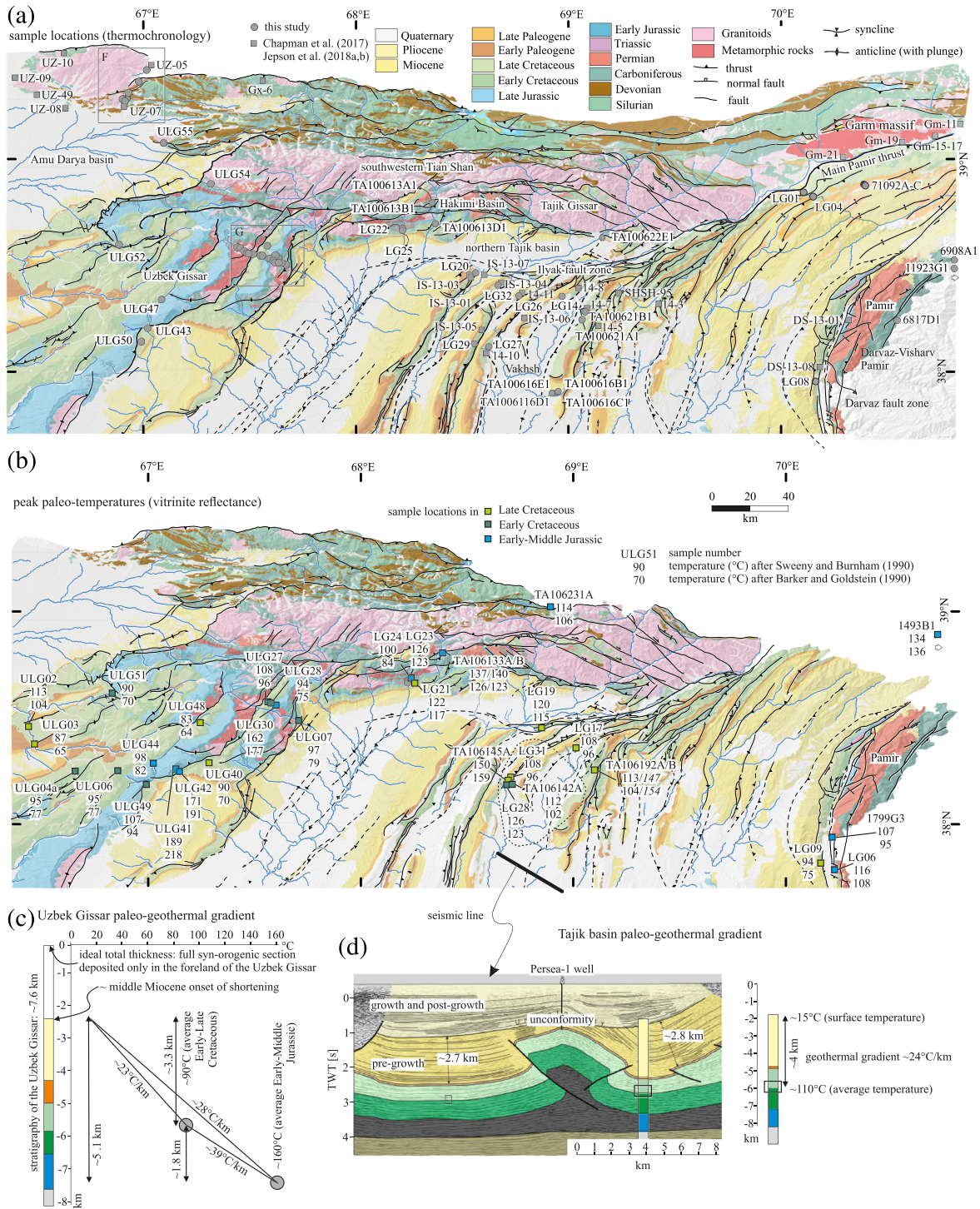


Figure 3. Geologic-structural maps of the Tajik basin and Tajik and Uzbek Gissar in the southwestern Tian Shan. (a) Sample locations. (b) Paleo-temperature values (in °C) from vitrinite-reflectance maturity measurements. (c) Paleo-geothermal gradients for the Uzbek Gissar from measured stratigraphic thickness (Rubanov et al., 1963) and averaged paleo-temperature estimates. (d) Paleo-geothermal gradient for the Tajik basin from stratigraphic thickness measured in a seismic line (location see (b); Gaġala, 2014) and averaged paleo-temperature estimates from surface samples corresponding to the indicated sample interval. (e–g) Thermochronologic data. Rectangles mark the detailed age-data maps in (f) and (g) below.

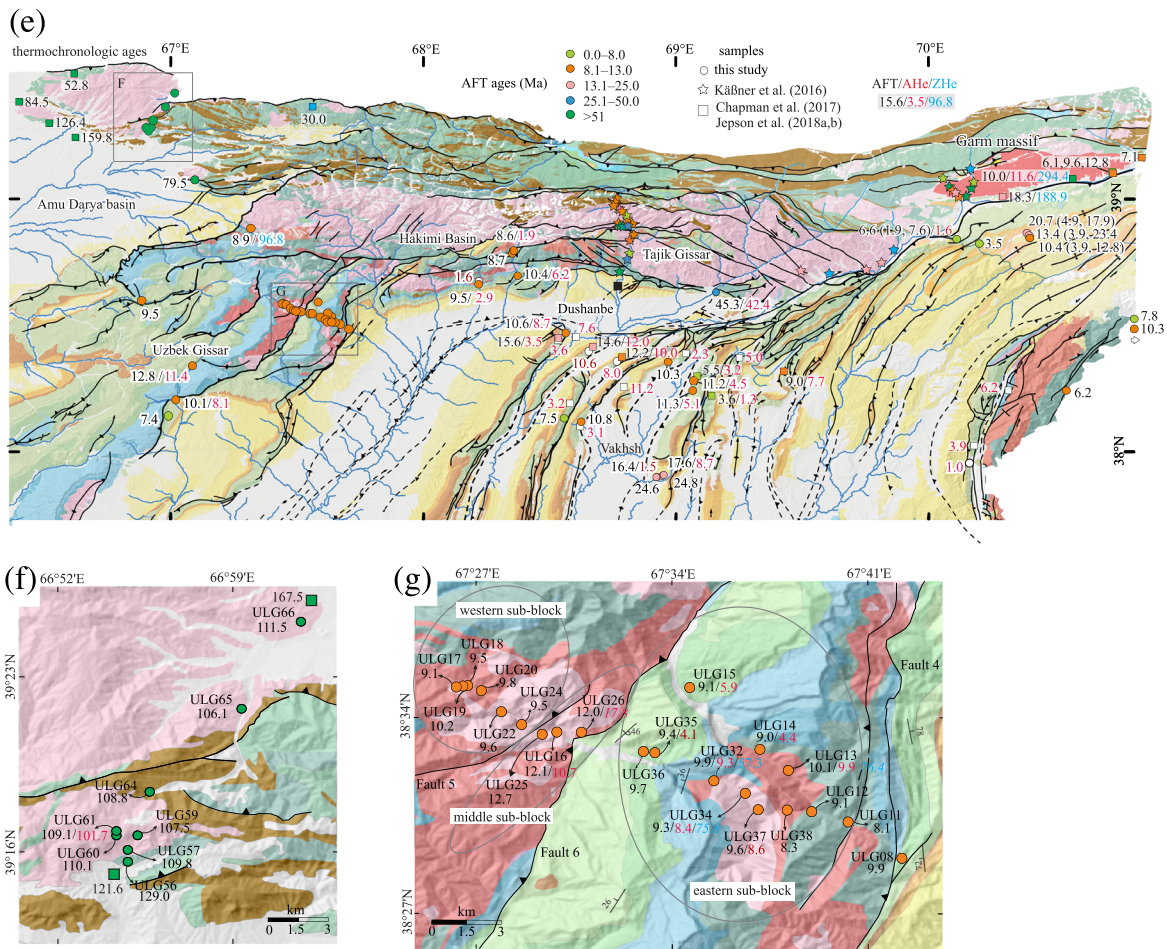


Figure 3. (continued)

chronometers record temperatures in the range of ~110–40 °C, depending on the cooling rate, grain size, and chemistry (e.g., Farley & Stockli, 2002; Green et al., 1986). We investigated eight Cr₁ and four Oligocene-Neogene sandstones from the north-central Tajik FTB, six Cr₁ sandstones from the northern Tajik-basin margin and the footwalls of thrusts bounding the intramontane Hakimi basin of the Tajik Gissar, three Cr₁ and three Oligocene-Neogene sandstones from the eastern part of the Tajik FTB, three metamorphic basement rocks from the western Pamir at the eastern margin of the Tajik basin (Darvaz-Visharv Pamir), 28 Cr₁ sandstones and crystalline basement rocks from the Uzbek Gissar, and eight crystalline rocks from a basement spur at the western edge of the southwestern Tian Shan. Table 1 gives the sample locations and lithologies and summarizes the new thermochronologic data; Figures 3a locates the samples and those published in the previous studies (Chapman et al., 2017; Jepson, Glorie, Konopelko, Gillespie, et al., 2018a; Jepson, Glorie, Konopelko, Mirkamalov, et al., 2018; Käßner et al., 2016); these data will be discussed together with the new ones (section 5.2).

The samples were processed for apatite and zircon. AFT ages and track lengths were determined following standard procedures in the Freiberg Track Laboratory, described in Wauschkuhn et al. (2015) and Käßner et al. (2016); Text S2 provides a summary. In essence, we liberated the grains by high-voltage-discharge rock fragmentation, etched the apatite mounts in 5.5 M HNO₃ at 21 °C for 20 s, and determined ages with the external detector method and the ζ calibration, using the Durango-apatite and IRMM-450R uranium-glass standards. Confined track-length measurements were done on separate mounts, using ¹³²Xe-ion irradiation to increase the number of measurable confined tracks. We applied thermal history (temperature-time [T-t]) modeling to samples with ≥ 33 measured confined tracks using HeFTy (Ketchum, 2005) and present the results as a set of 250 good-fit and acceptable-fit T-t solutions, and as contours of the node densities of 500 good-fit solutions for highlighting the changes in the T-t paths. Table S2 lists the AFT data.

Table 1
Sample Locations, Lithology, and Summary of Thermochronologic Data^a

Sample	Lithology	Latitude (N)	Longitude (E)	Elevation (m)	(U, Th)/He Age (Ma)	s.e. (1σ)	Apatite fission-track Age (Ma)	s.e. (± 1σ)
<i>Apatite</i>								
<i>Hakimi basin</i>								
TA100613A1	sandstone (Cr1)	38° 48.208'	68°21.836'	1,584	1.9	0.9	8.6	0.4
TA100613B1	sandstone (Cr1)	38° 46.977'	68°21.237'	1,507	n.a.	n.a.	8.7	0.4
<i>North-central Tajik basin</i>								
TA100613D1	sandstone (Cr1)	38°42.009'	68°22.053'	1,098	6.2	1.6	10.4	0.7
TA100616B1	sandstone (Pg3-N1; Baljuvon)	37°53.892'	68°56.446'	500	8.7	1.6	17.6	0.6
TA100616C1	sandstone (N1; base Khingou)	37°53.643'	68°56.147'	490	n.a.	n.a.	24.8	0.9
TA100616D1	sandstone (N1; Khingou)	37°53.443'	68°54.913'	465	n.a.	n.a.	24.6	1.0
TA100616E1	sandstone (N1; Khingou)	37°53.435'	68°54.794'	462	1.5	0.7	16.4	0.7
TA100621A1	sandstone (Cr1)	38°14.409'	69°03.371'	693	5.1	0.1	11.3	0.4
TA100621B1	sandstone (Cr1)	38°17.299'	69°03.694'	789	4.5	0.9	11.2	0.5
TA100622E1	sandstone (Cr1)	38°37.873'	69°09.435'	1,058	42.4	8.8	45.3	2.0
LG14	sandstone (Cr1)	38°20.885'	68°58.342'	865	n.a.	n.a.	10.3	1.8
LG20	sandstone (Cr1)	38°28.169'	68°33.804'	823	8.7	1.0	10.6	0.9
LG22	sandstone (Cr1)	38°39.914'	68°13.317'	1,067	1.6	0.1	n.a.	n.a.
LG25	sandstone (Cr1)	38°39.590'	68°13.405'	1,037	2.9	0.5	9.5	0.8
LG26	sandstone (Cr1)	38°20.463'	68°45.243'	1,342	8.0	1.2	n.a.	n.a.
LG27	sandstone (Cr1)	38°06.670'	68°36.836'	1,643	n.a.	n.a.	10.8	0.7
LG29	sand/siltstone (Cr1)	38°07.101'	68°33.428'	1,637	n.a.	n.a.	7.5	1.7
LG32	sand/siltstone (Cr1)	38°24.873'	68°41.224'	833	10.6	0.6	n.a.	n.a.
<i>Northeastern Tajik basin and Darvaz zone</i>								
LG01	silt-sandstone (Cr1)	38°51.070'	70°06.900'	1,367	1.6	0.4	6.6 ^b	0.5
LG04	sandstone (Cr1)	38°50.438'	70°09.118'	1,422	n.a.	n.a.	3.5	0.3
LG08	sandstone (Cr1)	37°56.705'	70°06.104'	915	1.0	0.4	n.a.	n.a.
71092A	sandstone (Pg3-N1; Baljuvon), lower section	38°53.738'	70°24.350'	2,371	n.a.	n.a.	20.7 ^b	1.3
71092B	sandstone (Pg3-N1; Baljuvon), middle section	38°53.675'	70°24.371'	2,289	n.a.	n.a.	13.4 ^b	1.1
71092C	sandstone (Pg3-N1; Baljuvon), upper section	38°53.536'	70°24.448'	2,269	n.a.	n.a.	10.4 ^b	0.6
<i>Sedimentary cover of Uzbek Gissar</i>								
ULG08	sandstone (Cr1)	38°28.914'	67°42.213'	891	n.a.	n.a.	9.9	1.1
ULG15	sandstone (Cr1)	38°34.977'	67°34.635'	1,589	5.9	0.4	9.1	0.6
ULG35	sandstone (Cr1)	38°32.648'	67°33.391'	1,255	4.1	0.5	9.4	0.8
ULG36	sandstone (Cr1)	38°32.690'	67°33.391'	1,266	n.a.	n.a.	9.7	0.8
ULG43	black siltstone/shale (J2)	38°12.328'	67°01.094'	1,029	8.1	1.1	10.1	0.6
ULG47	sandstone (Cr1)	38°22.196'	67°07.144'	1,404	11.4	2.3	12.8	0.8
ULG50	sandstone (Cr1)	38°07.343'	67°58.747'	1,088	n.a.	n.a.	7.4	0.7
ULG52	sandstone (Cr1)	38°35.604'	68°52.734'	1,002	n.a.	n.a.	9.5	1.2
<i>Crystalline basement rock of Uzbek Gissar</i>								
ULG11	meta-conglomerate (C1t2 + v1)	38°30.174'	67°40.286'	951	223.1	86.7	8.1	0.6
ULG12	meta-sandstone (C1t2 + v1)	38°30.541'	67°38.991'	999	n.a.	n.a.	9.1	0.5
ULG13	paragneiss	38°32.015'	67°38.154'	1,204	9.9	0.9	10.1	0.4
ULG14	quartz-rich micaschist	38°32.764'	67°37.14'	1,275	4.4	0.6	9.0	0.5
ULG16	orthogneiss	38°33.384'	67°29.886'	1,385	10.7	0.8	12.1	0.6
ULG17	leucogranite	38°35.049'	67°26.701'	1,521	n.a.	n.a.	9.1	2.0
ULG18	amphibolite	38°35.033'	67°26.531'	1,567	n.a.	n.a.	9.5	0.5
ULG19	felsic meta-volcanic rock (~350 Ma)	38°34.997'	67°26.295'	1,647	n.a.	n.a.	10.2	0.7
ULG20	granitoid	38°34.866'	67°27.186'	1,509	n.a.	n.a.	9.8	0.5
ULG22	granitoid	38°34.116'	67°27.902'	1,527	n.a.	n.a.	9.6	0.7
ULG24	granitoid	38°33.654'	67°28.629'	1,440	n.a.	n.a.	9.5	1.2
ULG25	Paleozoic metasandstone	38°33.399'	67°29.045'	1,423	n.a.	n.a.	12.7	1.5
ULG26	Paleozoic paragneiss	38°33.116'	67°30.78'	1,321	17.8	1.3	12.0	0.6
ULG32	granitoid (~355 Ma)	38°31.814'	67°35.413'	1,155	9.3	0.9	9.9	1.2
ULG34	leucocratic gneiss	38°31.193'	67°36.621'	1,105	8.4	0.8	9.3	0.4
ULG37	two-mica orthogneiss	38°30.611'	67°37.079'	1,086	8.6	0.4	9.6	0.4

Table 1
(continued)

Sample	Lithology	Latitude (N)	Longitude (E)	Elevation (m)	(U, Th)/He Age (Ma)	s.e. (1 σ)	Apatite fission-track Age (Ma)	s.e. (\pm 1 σ)
ULG38	aplitic gneiss	38°30.601'	67°38.115'	1,035	n.a.	n.a.	8.3	0.5
ULG54	orthogneiss (~336 Ma)	38°53.089'	67°17.592'	1,567	n.a.	n.a.	8.9	1.0
<i>Basement spur at the western edge of the southwestern Tian Shan</i>								
ULG55	schist (C)	39°04.192'	67°05.211'	1,105	n.a.	n.a.	79.5	6
ULG56	slate	39°15.48'	66°54.890'	1,053	n.a.	n.a.	129.0	10.1
ULG57	granite (~302 Ma)	39°16.076'	66°54.782'	1,139	n.a.	n.a.	109.8	3.5
ULG59	granite	39°16.653'	66°55.203'	1,349	n.a.	n.a.	107.5	3.7
ULG60	granite (~295 Ma)	39°16.655'	66°54.367'	1,450	n.a.	n.a.	110.1	4.3
ULG61	granite (~292 Ma)	39°16.832'	66°54.371'	1,542	101.7	6.9	109.1	3.8
ULG64	granite	39°18.335'	66°55.715'	1,462	n.a.	n.a.	108.8	3.4
ULG65	granite	39°21.639'	66°59.442'	1,041	n.a.	n.a.	106.1	4.1
ULG66	granite (~278 Ma)	39°25.171'	66°01.592'	961	n.a.	n.a.	111.5	4.0
<i>Darvaz-Visharv Pamir</i>								
6817D1	meta-andesite (C1)meta-andesite (C1)	38°14.405'	70°32.545'	1,115	n.a.	n.a.	6.2	0.5
6908A1	paragneiss (?Early Paleozoic)	38°25.912'	70°55.668'	1,337	n.a.	n.a.	7.8	0.4
11923G1	micaschist (?Early Paleozoic)	38°27.507'	70°57.597'	1,356	n.a.	n.a.	10.3	0.6
<i>Zircon</i>								
<i>Uzbek Gissar</i>								
ULG13	paragneiss	38°32.015'	67°38.154'	1,204	76.4	38.1	10.1	0.4
ULG32	granitoid (~355 Ma)	38°31.814'	67°35.413'	1,155	57.3	2.7	9.9	1.2
ULG34	leucocratic gneiss	38°31.193'	67°36.621'	1,105	75.8	20.0	9.3	0.4
ULG54	orthogneiss (~336 Ma)	38°53.089'	67°17.592'	1,567	96.8	9.7	8.9	1.0

^an.a., not analyzed; Cr, Cretaceous; C, Carboniferous. ^bLGO1: age groups at 1.9 ± 0.6 , 7.6 ± 1.1 , 33.4 ± 7.6 Ma; 71092A: age groups at 4.9 ± 0.9 , 17.9 ± 1.9 , 54.7 ± 5.6 , 498 ± 126 Ma; 71092B: age groups at 3.9 ± 0.6 , 23.4 ± 4.8 , 84 ± 15 Ma; 71092C: age groups at 3.9 ± 0.5 , 12.8 ± 2.0 , 39.7 ± 5.4 Ma.

We performed AHe and ZHe measurements with the Patterson He-extraction line at the Universität Tübingen, Germany, following the procedures summarized in Käbner et al. (2016); Text S3 provides a summary. We picked clear idiomorphic grains free of inclusions, impurities, or cracks and measured their dimensions for calculating the α -correction factors (Farley et al., 1996). Two to five single grains per sample were degassed, reheated, and remeasured to check for complete degassing. U, Th, and Sm were measured at the University of Arizona. We report the unweighted arithmetic mean and standard error of the grain ages as the AHe and ZHe sample ages and their uncertainties. Table S2 lists the AHe and ZHe data.

4. Results

Figure 3a presents a structurally interpreted geologic map of the Tajik basin and southwestern Tian Shan with the sample locations of the new and published (Chapman et al., 2017; Käbner et al., 2016; Jepson, Glorie, Konopelko, Gillespie, et al., 2018a; Jepson, Glorie, Konopelko, Mirkamalov, et al., 2018) thermochronologic data. Figure 3b shows the regional distribution of paleo-temperatures, and Table S1 gives the results for the different stratigraphic horizons and regions. Overall, the temperatures follow the down-depth trend: the paleo-temperature values for the Cretaceous (Cr₁₊₂) strata are 89°/103 °C (first and second numbers give calculation after Barker & Goldstein, 1990 and Sweeney & Burnham, 1990, respectively) and 132/132 °C for the Early-Middle Jurassic strata. In the Tajik basin, the values for the Cr₂ strata—103/108 °C—are close to those of the Cr₁ strata (113/119 °C). The data from the Tajik Gissar—covering Jurassic rocks—are only slightly higher (115/121 °C). Again, the values for the Cr₂ (75/93 °C) and Cr₁ (81/98 °C) strata of the Uzbek Gissar are nearly identical but lower than those of the Tajik basin. The highest, albeit variable paleo-temperatures (167/155 °C) occur in the Jurassic rocks of the Uzbek Gissar. The values (75/94 °C, Cr₂

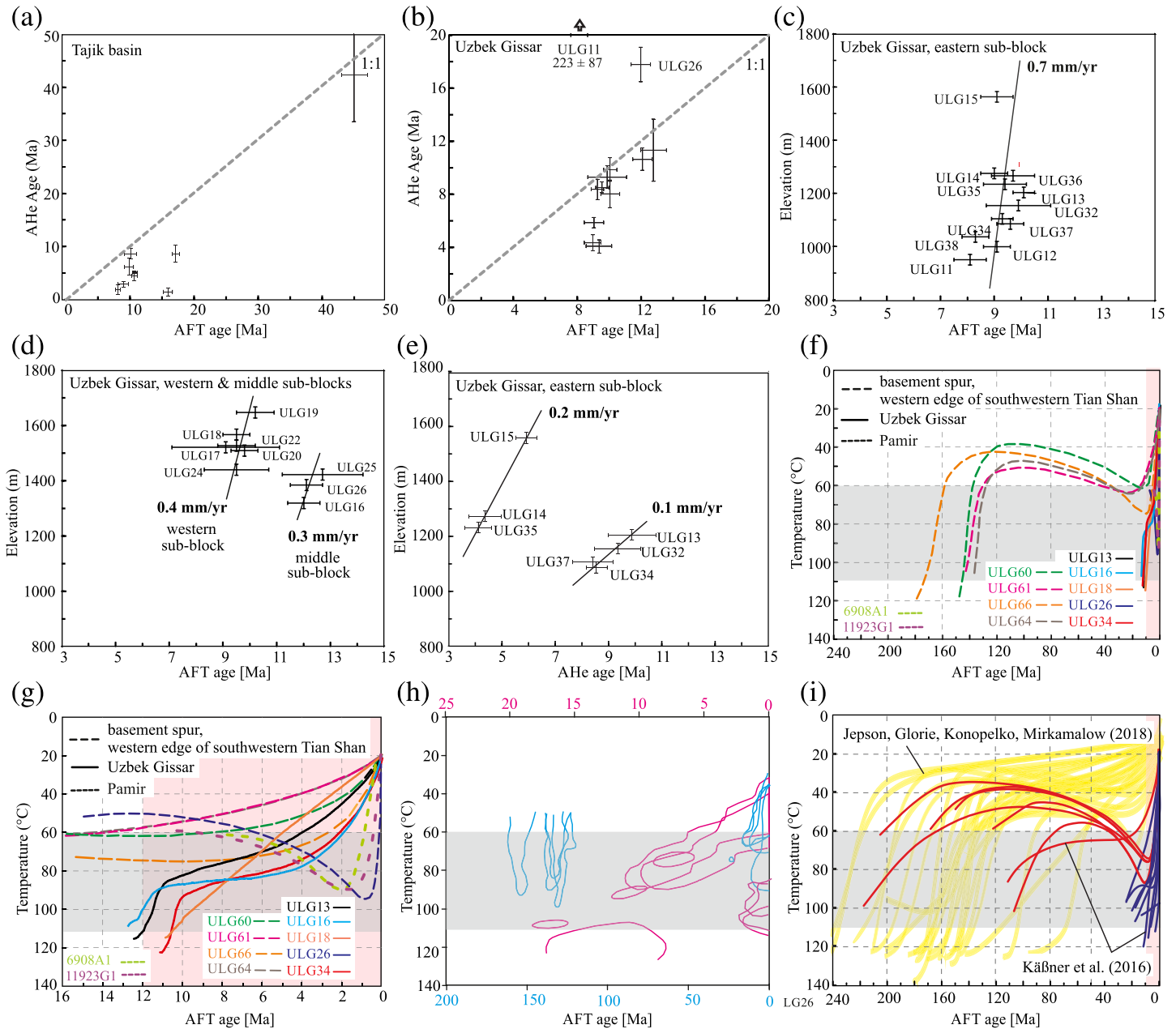


Figure 4. (a and b) Apatite (U, Th)/He (AHe) ages plotted against apatite fission-track (AFT) ages for the Tajik basin and the Uzbek Gissar. (c) AFT age versus elevation plot for the eastern and (d) middle and western subblocks of the Uzbek Gissar. (e) AHe age versus elevation plot for the eastern subblock of the Uzbek Gissar. (f and g) Weighted mean temperature-time (T-t) paths of the AFT thermal history models in Figure S4. (h) 90% contours of the T-t path node densities of all good-fit thermal histories, highlighting where cooling-rate changes occur (see Text S2 and Figure S4 for details). The blue contours relate to the age scale at bottom and the magenta ones to that at top. T-t paths for the Tajik Gissar samples. The gray sectors in (f), (g), and (i) represent the AFT partial annealing zone; the pink fields indicate rapid cooling.

strata; 113/119 °C Lower-Middle Jurassic strata) are relatively low along the margin to the Pamir (Darvaz range).

Figures 3c and 3d show attempts to derive paleo-geothermal gradients for the Uzbek Gissar and the Tajik basin, respectively. For the estimate visualized in Figure 3c, we averaged the paleo-temperature values from the Cr₁-Cr₂ and Lower-Middle Jurassic rocks and used the detailed strata-thickness measurements of

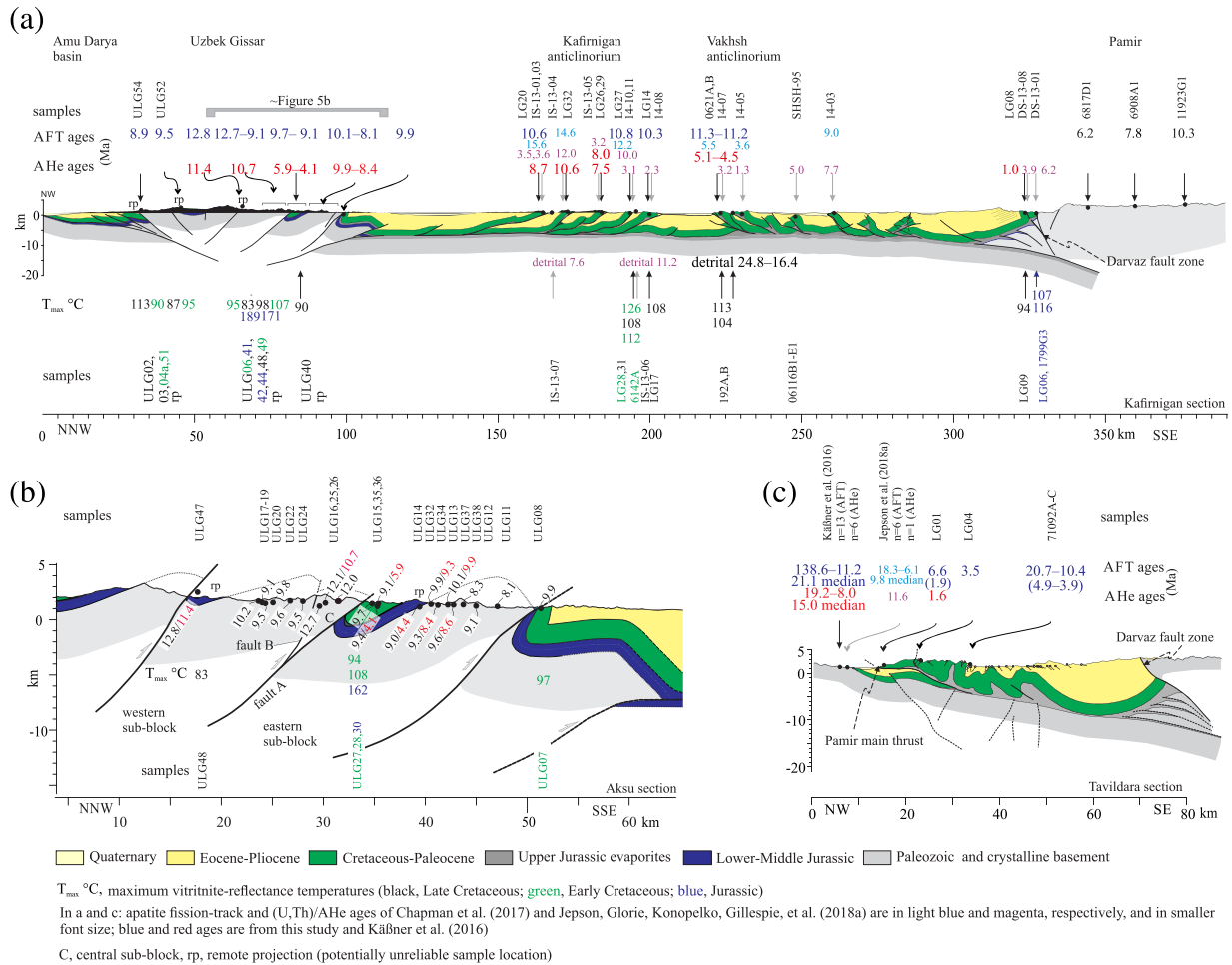


Figure 5. (a) Kafirnigan cross section through the Tajik basin and Uzbek Gissar simplified from Gagała et al. (2020) with paleo-temperature values derived from the Sweeney and Burnham (1990) calibration, and new and published apatite fission-track (AFT) and (U, Th)/He (AHe) ages projected along strike onto the section. (b) Section across the eastern Uzbek Gissar based on detailed mapping; location is farther south than section in (a) to best show the faults and subblocks of Figures 3f and 3g discussed in the text. For cross-section lines see Figure 1b. Our new age data and those of Käßner et al. (2016) are in dark blue (AFT) and red (AHe); those of Chapman et al. (2017) and Jepson, Glorie, Konopelko, Gillespie, et al. (2018a) are in light blue (AFT) and magenta (AHe) and smaller font size.

Rubanov et al. (1963). Based on our thermochronology (see below), we assumed that burial reversed to uplift and erosion at ~12 Ma, that is, the middle Miocene, thus giving a minimum of overburden, because sedimentation likely continued in synclines and away from growing anticlines; furthermore, we assumed that average surface temperature was at ~15 °C. We derived maximum paleo-geothermal gradients of ~39 °C/km for the Cretaceous-Jurassic section, ~23 °C/km for the Cretaceous-Miocene section, and ~28 °C/km for the Jurassic-Miocene section (Figure 3c); given the variable Jurassic paleo-temperature estimates, a 25–30 °C/km value may apply for the Uzbek Gissar. For the Tajik basin, industrial seismic sections (Gagała, 2014) allow the identification of the boundary between the preorogenic and synorogenic strata and the strata thickness to the Cr₁-Cr₂ (on surface) sampling sites at several locations; the Tajik-basin gradient was at ~25 °C/km (Figure 3d).

The paleo-temperature estimates of the Lower-Middle Jurassic strata of the Uzbek Gissar are—with the exception of one outlier—>110 °C. Therefore, the AFT and AHe samples from these strata and the underlying crystalline basement rocks experienced a reset of their preexisting age record; they trace the youngest cooling event. The average paleo-temperatures of samples collected around the Cr₁-Cr₂ boundary scatter between ~75 and 125 °C; as a rule, higher values occur in the Tajik basin (115–125 °C) than the Uzbek Gissar (75–100 °C; Table S1). The thermochronologic sample localities in the Cr₁ clastic rocks are

stratigraphically ~0.5–1.0 km deeper, which implies ~10–30 °C higher temperatures. If so, the Cr₁ Tajik-basin rocks were reset, while those from the Uzbek Gissar may have been reset fully or partially.

Figures 3e to 3g present maps with the regional ZHe, AFT, and AHe age distribution; the AFT ages are color-coded to emphasize age ranges. Table S2 details the AFT-age and mean track-length data. Figure S2 presents radial plots (Galbraith, 1990) of the apatite single-grain ages. Table S3 lists the He, U, Th, and Sm concentrations and single-grain parameters, and Figure S3 plots the single-grain AHe ages against their equivalent uranium concentrations (eU) and grain widths. We used the data in Figure S3 and Table S3 to detect outliers (bold in Table S3), which were not included in the mean AHe-age calculations. Figure 4 compares the AFT and AHe ages (Figures 4a and 4b), plots the AFT and AHe ages versus elevation (Figures 4c to 4e), shows T-t modeling results (Figures 4f to 4h), and compares these with the results of Käßner et al. (2016) for the Tajik Gissar and Jepson, Glorie, Konopelko, Mirkamalov, et al. (2018) for the Kyzylkum-Nurata segment of the northwestern-most Tian Shan (Figures 1b and 4i). Figure S4 shows the track-length distributions and full modeling solutions of our samples. Data Set S1 in the supporting information compiles the dates of Jepson, Glorie, Konopelko, Gillespie, et al. (2018a) for the Garm massif of the Tajik Gissar, and Jepson, Glorie, Konopelko, Mirkamalov, et al. (2018) for the basement spur at the western edge of the southwestern Tian Shan, which overlap with our ages; for completeness, it also includes the dates of Chapman et al. (2017) for the Tajik basin. In Figure 5, we projected the paleo-temperature and thermochronologic data along strike into simplified versions of the Kafirnigan and Tavildara cross sections of Gağala et al. (2020); the section of Figure 5b details the structures and ages in the eastern Uzbek Gissar. In general, the youngest AFT ages occur east of the present margin of the Tajik basin in the westernmost Pamir and along the leading edge of the Pamir thrust system—the Vakhsh thrust—of the northeastern Tajik basin, where it narrows between the converging Tian Shan and Pamir. The Vakhsh anticlinorium in the east-central part of the Tajik basin and, in particular, the Darvaz fault zone and the Pamir thrust system yielded the youngest AHe ages (Figures 3e, 5a, and 5c).

The new AFT ages in the north-central Tajik basin, along its northern margin, and in the Hakimi basin of the Tajik Gissar, range from ~45.3 to 7.5 Ma (Figure 3e and Table 1). Figure S2 shows that the single-grain ages of the four samples from the Neogene rocks are consistent with their sample ages (Table 1; ~24.8–16.4 Ma, median = 21.1 Ma). The sample ages are somewhat higher than or close to the upper limit of the depositional age range (three samples from the Khingou Formation with a stratigraphic age of ~18–12 Ma and one sample from the Baljuvon Formation with a stratigraphic age of ~28–18 Ma; see discussion on the difficult stratigraphic age assignment for these Formations in Klocke et al., 2017 and Dedow et al., 2020). The single-grain ages of the samples from the Cr₁ rocks are also consistent with their sample ages. These samples have much lower ages (~11.3–7.5 Ma; median = 10.4 Ma; $n = 10$) than their stratigraphic age, which implies postdepositional resetting. Their ages are also much lower than the AFT ages of the Neogene rocks, suggesting that these were not reset. The only outlier—TA100622E1—was sampled just south of basement rocks at the northern margin of the Tajik basin (Figure 3e); its ~45-Ma AFT age is intermediate between its stratigraphic age and the exhumation age of the other samples from the Cr₁ rocks (~10.4 Ma).

Two AFT ages from Cr₁ rocks in the hanging wall of the Vakhsh thrust in the northeastern Tajik basin are ~6.6 and 3.5 Ma (Figures 3e and 5c; Table 1). Whereas sample LG04 has single-grain dates consistent with its sample age (~3.5 Ma), sample LG01 (~6.6 Ma) contains two single-grain dates that overlap the depositional age; the remaining dates may define age peaks at ~1.9 (33% of the population), 7.6 (53%), and 33.4 Ma (14%) (Figure S2). The youngest age peak of LG01 (~1.9 Ma), sampled just south of the thrust front, is little older than the AHe age of this sample (~1.6 Ma). Three samples (71092A–C) of upper Oligocene-lower Miocene Baljuvon-Formation (stratigraphic age of ~28–18 Ma) rocks from the southward overturned limb of a huge anticline cored by a salt ridge (Figure 5c) have single-grain dates both older and younger than the stratigraphic age, indicating partial resetting (Figure S2). The youngest age peaks of all three samples (~4.9–3.9 Ma, comprising 28–55% of the population) may represent fully reset ages; they are only slightly older than the age from the Cr₁ strata (LG04, ~3.6 Ma) in the syncline closer to the thrust front (Figure 5c).

The 26 sample ages from the Uzbek Gissar (both sedimentary cover and crystalline basement rocks) cover ~12.8–7.4 Ma (median = 9.6 Ma; Figure 3e and Table 1). Those from the basement spur at the western edge

of the southwestern Tian Shan are distinctly older: ~129–80 Ma (median = 109 Ma, $n = 9$); the youngest is farthest south and in the hanging wall of a thrust emplacing basement onto Neogene rocks.

The AFT ages are older than the corresponding AHe ages, except for ULG11 and ULG26 (Figures 4a and 4b). We consider the AFT ages of these two samples more reliable because they agree with the rest of the AFT samples, and discard the AHe ages, which do not. In addition, the individual grain AHe ages of ULG11 differ by an order of magnitude, and the ~223-Ma mean age is even older than the ZHe ages from this region (see below). Eleven AHe ages within the north-central Tajik basin, along its northern margin, and in the Hakimi basin range from ~10.6 to 1.5 Ma (median = 6.2; Figure 3e and Table 1). TA100622E1 (~42 Ma) is—as it was the case for the AFT age—much older than the other samples. Young AHe ages—LG08 (1.0 Ma) and LG01 (1.6 Ma)—occur along the Darvaz fault zone in the easternmost part of the Tajik basin, and—as mentioned above—at the frontal thrust of the Pamir thrust system (Figures 3e and 5c). Ten AHe ages from the Uzbek Gissar range from ~11.4 to 4.1 Ma (median = 8.5 Ma). The four ZHe ages from this region range between ~97 and 57 Ma (Table 1).

The number of samples and elevation ranges within a single thrust sheet are too small for estimating exhumation rates from age-elevation data in the Tajik basin. Figures 4c to 4e show age-elevation plots for three fault-bounded blocks in the Uzbek Gissar (see Figure 3g for their definition). Although there are several samples per block, the small elevation ranges and the considerable horizontal distances between the samples negate the use of age-elevation relationships. Other factors that we cannot assess thoroughly, for example, burial by synorogenic strata in synclines or by local thrusting during exhumation, invalidate or modify the results. We show them for completeness of analysis, but the derived exhumation rates are at best order-of-magnitude estimates. The rates calculated from error-weighted regressions, assuming ± 20 -m uncertainties on the GNSS-derived elevations, are ~0.7, 0.3, and 0.4 mm/year for the eastern, middle, and western block, respectively. Only the eastern block provided enough AHe ages for calculating an exhumation rate (Figure 4e). Two age groups can be distinguished: Samples with AHe ages between ~4.1 and 5.9 Ma give an exhumation rate of ~0.2 mm/year, those with AHe ages between ~8.4 and 9.9 Ma give ~0.1 mm/year. The former estimate is consistent with the values calculated from the offset between the AFT and AHe ages (0.2–0.6 mm/year, for a geothermal-gradient range of 20–30 °C/km and 1.3–2.0 km difference in the depth of the closure paleo-isotherm). The exhumation-rate estimate for the older group gives rates >1 mm/year, as expected given the small offset between the AFT and AHe ages of these samples; the much lower rate estimate (~0.1 mm/year) from the age-elevation relation is therefore deemed questionable due to the small elevation difference between the samples. Taking all AFT and AHe ages (~2.5-Ma age difference) from all blocks of the Uzbek Gissar yields 0.5–0.8 mm/year of exhumation.

Figures 4f and 4g show the mean T-t paths for the modeling solutions in Figure S4; Figure 4h displays 90% contours of the T-t-path node densities, highlighting cooling-rate changes. The modeled samples are from the Uzbek Gissar (ULG13, 16, 18, 26, and 34; ~12.1–9.3 Ma), the basement spur at the western edge of the southwestern Tian Shan (ULG60, 61, 64, and 66; ~112–108 Ma), and the Pamir east of the Tajik basin (6908A1 and 11923G1; ~7.8 and 10.3 Ma; Table 1). Two T-t-path groups are apparent: The samples from the basement spur cooled through the AFT partial annealing zone (PAZ) between ~160 and 130 Ma were reheated to ~80–60 °C between ~40 and 15 Ma and cooled to surface temperature from ~10 Ma onward. The samples from the Uzbek Gissar entered the PAZ at ~1311 Ma; ULG13, 16, and 34 then cooled through the PAZ between ~11 and ~2 Ma; ULG18 cooled to surface temperature from ~11 Ma onward. Both groups experienced accelerated cooling since ~10 Ma. These T-t paths contrast with that of sample ULG26 (~12.0 Ma) from the Uzbek Gissar and those of the two western Pamir samples (6908A1, ~7.8 Ma; 11923G1, ~10.3 Ma); they apparently cooled through the PAZ before ~10 Ma, reentered the PAZ until ~2 Ma, and cooled rapidly to surface temperature (Figure 4g). The AHe age of ULG26 is unreliable (see above) and thus not helpful for evaluating the T-t path. The data from the closest neighboring sample ULG16 (Figure 3g) show a distinctly different T-t path (see above) and an AHe age (~10.6 Ma) incompatible with the ULG26 path. In contrast, the AHe age (~1.0 Ma) from the easternmost Tajik basin is compatible with the T-t paths of the adjacent Pamir samples. The two Cr₁ samples with track lengths from the Tajik basin have too few tracks for T-t path modeling. Sample TA100621A1 (~11.3 Ma) has a mean track length (~13.4 μm , $n = 13$) identical to the length of the Uzbek Gissar crystalline basement samples. Sample LG04 (~3.5 Ma) from the Pamir thrust front has a shorter mean track length (~11.6 μm , $n = 23$). Both mean

lengths are larger than the partially reset Cr₁ sample TA100622E1 (~10.7 μm) and the partially reset upper Oligocene-lower Neogene sample 71092B (~8.3 μm).

5. Discussion

We set out to extend the “northward indentation-westward flow” tectonic model of the active deformation field at the northwestern tip of the India-Asia collision (Kufner et al., 2018; Schurr et al., 2014), to investigate its onset and duration, and to integrate the tectonics of the Pamir, Tajik basin, and southern Tian Shan. In the following, we address three questions: (1) When were the Tajik basin and the southwestern Tian Shan inverted to form the thin-skinned Tajik FTB and its thick-skinned foreland buttresses? (2) Is there a time progression? (3) How were inversion of the Tajik basin and shortening in the Tian Shan coupled with the hinterland—the Pamir?

5.1. Onset and Duration of Shortening in the Uzbek and Tajik Gissar and Inversion of the Tajik Basin

Several first-order observations result from the ages and the distribution of the ZHe, AFT, and AHe ages across the present structure of the Uzbek Gissar. First, the ~97- to 57-Ma ZHe ages in the Uzbek Gissar refer to a closure temperature of ~140–180 °C (Reiners et al., 2004), using the estimated pre-Cenozoic cooling rates of 0.01–10 °C/Myr (Käßner et al., 2017). This implies that Cenozoic burial did not reheat the apatites far above their AFT PAZ temperatures. Second, and foremost, the AFT ages are relatively uniform despite being distributed over a thickness interval of up to 5 km in the thrust sheets that define the western and eastern subblocks (Figure 5b). This indicates that the sampled depth intervals passed through the AFT PAZ nearly simultaneously, constraining the onset of inversion to ≥12.8 Ma—the oldest AFT age (range of all data ~12.8–7.4 Ma, median = 9.6 Ma; Figures 3e, 5a, and 5b). The samples in the core of the anticlines of the eastern and western subblocks were the deepest and hottest (Figure 5b). Their ages young downward (toward the core of the anticlines), becoming as young as ~8.1 Ma; they likely postdate the onset of thrusting. The AHe ages can be divided in an older (~11.4–8.4 Ma) and a younger (~5.9–4.1 Ma) subset. The older AHe ages are close to the AFT ages and indicate rapid (>1 mm/year) exhumation to ~2- to 3-km depth soon after the onset of shortening. The younger AHe ages occur in the syncline in the footwall of the major thrust in the western part of the eastern subblock (fault A in Figure 5b). Deposition of sediments in the syncline likely formed a—now eroded—piggyback basin. There, the AFT ages (~9.7–9.1 Ma) thus again date cooling due to thrusting and erosion and set a minimum age for the onset of shortening. The reheating or slowing of the long-term exhumation/cooling rate might explain the large offset between the AFT (~9.7–9.1 Ma) and AHe (~5.9–4.1 Ma) ages in this syncline (Figure 5b).

Four samples from the Uzbek Gissar have AFT ages ≥12 Ma (Table 1). One, from the Cr₁ sedimentary cover of the Uzbek Gissar, is the oldest (ULG47, ~12.8 Ma); it likely projects into the western subblock (Figure 5b). The other three are from the central subblock (~12.7–12.0 Ma, marked “C” in Figure 5b). These samples are ~1 Ma older than the other samples from the Uzbek Gissar and the oldest samples from the Tajik basin. Characteristically, the mean track lengths of these samples (ULG16: ~12.1 μm, *n* = 68; ULG26: ~9.9 μm, *n* = 43) are shorter than those of the younger samples (~13.3–12.8 μm, three samples, *n* = 97–116). The older samples could have been within the AFT PAZ, and today part of a fossil PAZ. This would explain both their older ages compared to the other samples and their shorter mean track lengths. This would also reconcile the problem that a full reset of the Cr₁ sample ULG47 is unlikely, given the ~83/60 °C (depending on the calibration) paleo-temperature for the close-by Cr₂ vitrinite sample ULG48. The implication—that the ≥12 Ma ages overestimate the onset of shortening—is appealing: if so, the ages from the Uzbek Gissar, Tajik Gissar, and the Tajik basin (see below) all together suggest an ~12-Ma age for the onset of shortening and erosion.

The AFT and AHe samples from the Tajik basin are from Cretaceous and upper Oligocene-lower Neogene sandstones. All ages of the Cretaceous samples were reset, while those from Oligocene-Neogene samples are not or partly reset (Figure S2 and Table S2). This agrees with the vitrinite-reflectance paleo-temperatures (~106/115 °C, average of the Cretaceous samples, depending on the calibration). The Cr₁ clastic rocks sampled for thermochronology are situated stratigraphically ~0.5–1.0 km deeper than the samples for paleo-temperature, that is, at 10–30 °C higher temperatures. At these temperatures, the samples

were reset and cooled through the PAZ immediately after the onset of thrusting and erosion. The relative uniform AFT ages (~11.3–7.5 Ma, median = 10.4 Ma) of the Cr₁ samples across the north-central Tajik basin indicate that inversion started at ~12 Ma, likely more or less simultaneously along all structures (Figures 3e and 5a). The oldest AHe ages (~10.6–8.0 Ma) are only slightly younger, implying exhumation to ~2- to 3-km crustal depths within a few Myr. The two AFT ages from Cr₁ rocks in the hanging wall of the Vakhsh thrust in the northeastern Tajik basin are much younger, ~6.6 and 3.5 Ma (Figures 3e and 5c and Table 1), consistent with the high seismicity and the ~15-mm/year GNSS-derived shortening rates across this dextral-reverse fold-thrust system (Ischuk et al., 2013; Kufner et al., 2018). The reason for the presence of clusters in the single-grain dates of sample LG01 (pooled age ~6.6 Ma) at ~1.9 (33% of the population), 7.6 (53%), and 33.4 Ma (14%) is unclear but may reflect incomplete resetting and compositionally variable apatite grains. The youngest age peak of LG01 (~1.9 Ma), sampled just south of the thrust front, and likely comprising fully reset grains, is little older than the AHe age of this sample (~1.6 Ma). These young ages likely reflect the active syntectonic erosion of the evaporite-soleid deformation front of the Tajik FTB along the Vakhsh thrust by the Surkhob longitudinal trunk stream (cf. Pavlis et al., 1997), with the older AFT age in the imbricate closer to the hinterland (LG04, ~3.5 Ma; Figure 5c).

The AFT and AHe ages, ~10.4–8.6 and ~6.2–1.6 Ma, respectively, in northern Tajik basin and western Tajik Gissar indicate a similar age for the shortening/erosion-induced cooling for these areas than for the north-central Tajik basin (south of the Ilyak fault zone; Figure 3e). As Käßner et al. (2016) outlined for the Tajik Gissar farther east, the southwestern Tian Shan is an integral part of the Pamir deformation field, dominated by dextral transpression. Together with the Ilyak fault zone, it constitutes the northern thick-skinned foreland buttress of the thin-skinned Tajik FTB (Gağala et al., 2020; Kufner et al., 2018). Similar ages and structures (Figures 1c and 3a) extend this zone along-strike to the west. The old AFT (~45 Ma) and AHe ages (~42 Ma) of sample TA100622E1 can be understood in connection with the data of Käßner et al. (2016). The basement block of the Tajik Gissar adjacent to the Tajik basin yielded AFT ages between ~86 and 6 Ma and AHe ages between ~26 and 5 Ma, indicative of partial Cenozoic resetting. TA100622E1 traces the same signal that delineates a relatively rigid block, moderately deformed and exhumed during the Neogene (Figure 3e; Figure 4 in Käßner et al., 2016).

We interpret the unreset AFT ages (~24.8–16.4 Ma) of the upper Oligocene-middle Miocene samples from the north-central Tajik basin (TA100616B1–E1) as the detrital signal of the Central and South Pamir. There, crustal thickening and accompanying erosion peaked at ~23–20 Ma, followed by tectonic denudation forming the extensional gneiss domes (section 1; Hacker et al., 2017; Rutte, Ratschbacher, Khan, et al., 2017). The upper Oligocene-middle Miocene Baljuvon and Khingou Formations of the north-central Tajik basin thus possessed a drainage network extending deep into the Pamir with a short lag time between exhumation, erosion, and deposition. In contrast, the three samples (71092A–C) of upper Oligocene-lower Miocene Baljuvon-Formation rocks of the Pamir thrust system of the northeastern Tajik basin (Figures 3e and 5c) have single-grain AFT ages both older and younger than the stratigraphic age. The youngest age peaks of all three samples (~4.9–3.9 Ma, 28–55% of the population) may represent fully reset ages; they are only slightly older than the age from the Cr₁ strata (LG04, ~3.6 Ma) in the syncline closer to the thrust front (Figure 5c). Together these ages imply young shortening/focused erosion along the Pamir thrust system, consistent with the narrowing of the Tajik basin to its northeast.

Käßner et al. (2016) obtained AFT and AHe age ranges of ~238.6–11.2 Ma (median = 21.2 Ma) and ~19.2–8.0 Ma (median = 15.0 Ma), respectively, from the crystalline basement rocks of the Tian Shan foreland buttress immediately north of the Vakhsh thrust; Jepson, Glorie, Konopelko, Gillespie, et al. (2018a); see discussion of their data in section 5.2) reported AFT ages that span ~18.3–6.1 Ma and one AHe age at ~11.6 Ma for the southern edge of the Garm massif, east of the study area of (Käßner et al. (2016); Figures 3e and 5c). These AFT and AHe ages from the southern rim of the Tian Shan foreland buttress are mostly from a fossil partial annealing/retention zone and imply vastly different amounts of shortening and exhumation on both sides of the Vakhsh thrust. Both the difference in the cooling ages (~10 Ma; Figure 3e) and in the stratigraphic thicknesses of the fully preserved Cretaceous-Oligocene stratigraphic sections across the Vakhsh thrust (~700 m to its north and ~2,500 m to its south; Burmakin et al., 1961; Gağala et al., 2020) imply that different parts of the Tajik basin have been juxtaposed across this thrust front. This supports Pavlis et al. (1997) model of large-scale evacuation of rocks from the thrust front by river erosion.

Our T-t models for the basement spur at the western edge of the southwestern Tian Shan indicate cooling through the AFT PAZ between ~160 and 130 Ma, followed by reheating to ~80–60 °C between ~40–10 Ma (Figure 4f). Käßner et al. (2016) reported similar, albeit more heterogeneous (~200–80 Ma) histories for parts of the Tajik Gissar (Figure 4i). Furthermore, Jepson, Glorie, Konopelko, Mirkamalov, et al. (2018) T-t models for the Kyzylkum-Nurata segment of the northwestern-most Tian Shan—including the basement spur at its southeastern tip—indicate cooling through the PAZ between ~220–60 Ma, with a cluster between ~160 and 120 Ma (yellow paths in Figure 4i). Their only model that indicates reheating (between ~40 and 15 Ma) into the PAZ is from the basement spur, which also shows relative young ages, including an ~30 Ma date from farther east (Figure 3e). Also, parts of the Chatkal-Kurama range north of the Fergana basin show this reheating (Jepson, Glorie, Konopelko, Gillespie, et al., 2018). Taking all data together, this suggests that the basement spur constitutes a relatively rigid block—shallowly buried and exhumed during the Cenozoic in comparison to the Tajik and Uzbek Gissar. The Jurassic-Cretaceous cooling recorded in the western Tian Shan likely is the vestige of widespread crustal extension after the “Eo-Cimmerian” (Norian-Rhaetian) orogeny, best documented in Uzbekistan and Iran. Extension almost ceased at the end of the Middle Jurassic (~160 Ma), with only minor normal faulting recorded in Upper Jurassic and Cretaceous strata; this time was mostly characterized by thermal subsidence (e.g., Brunet et al., 2017; Fürsich et al., 2015; Mordvintsev et al., 2017). For the often cited trigger of the cooling by collisions at the southern margin of Asia (e.g., De Grave et al., 2012, 2013; Glorie et al., 2011; Jepson, Glorie, Konopelko, Gillespie, et al., 2018), we see no structural evidence in the studied areas. The Jurassic-Cretaceous cooling was later superimposed by burial heating, evidenced by the stratigraphic record, peaking with the deposition of the synorogenic sediments from the rising Pamir (and Tian Shan) in the Oligocene and mostly Miocene. Unsurprisingly, subsidence and reheating were highest in the Tajik basin, diminishing north(west)ward, leaving a weak reheating signal in the basement spur at the western edge of the southwestern Tian Shan and none in the Kyzylkum-Nurata segment of the northwestern-most Tian Shan. Similarly, we interpret the ZHe ages from the Uzbek Gissar and the basement spur at the western edge of the southwestern Tian Shan as relicts of Jurassic-Cretaceous events, partially reset by Cenozoic burial.

How can we interpret the different T-t paths of samples ULG26 (Uzbek Gissar) and 6908A1 and 11923G1 (northwestern Pamir; Figure 4g)? We have found no meaningful interpretation for ULG26. On the one hand, the relatively high proportion of short tracks allows us to speculate about methodologic factors, that is, track-etching or track-measurement-related issues; on the other hand, the fact that this sample is from the core of a fault zone hints at tectonic causes, for example, fluid flow along the fault. In the northwestern Pamir, the upper Miocene-Pliocene sedimentary rocks of the Tavildara and Karanak Formations, and in particular those of the Pliocene-Pleistocene Polizak Formation, cover an erosional surface southeast of the Darvaz fault zone, filling bedrock topography (Klocke et al., 2017; Lyoskind et al., 1963 own observations). This indicates a period of subsidence with transgression of the Tajik basin far onto the North Pamir interior. Burial by ~1 km of sediments could have caused the observed upper Miocene-Pliocene reheating before either a renewed pulse of shortening or incision by the Panj River (headwater of the Amu Darya) exhumed the rocks to the surface. The preservation of these Formations at altitudes of 3.2- to 3.5-km points to young regional uplift of the eastern Tajik basin and adjacent Pamir. On the one hand, the river incision interpretation is appealing given the ~2 km of downcutting of the Panj River gorge. On the other hand, the young AHe age at a relatively high elevation along the Darvaz fault zone (Figures 3e and 5a) may favor out-of-sequence tectonic shortening at the basin margin.

5.2. Time Progression of Shortening

Chapman et al. (2017) published a first set of AFT and AHe ages from the northern Tajik FTB. Are these data compatible with ours? Table S4 of Data Set S1 lists their ages, and Figures 3a, 3e, and 5a plot the sample locations and ages together with ours. To make the two data sets comparable, we report Chapman et al.'s (2017) AFT ages as pooled ages, and the AHe ages as unweighted mean ages; this has little effect on the original data. As a pioneering first study, Chapman et al.'s (2017) AFT thermochronology relies on a smaller database (see Tables S2 to S4). We also made small modifications to their AHe data set. In their fully reset Cr₁ sample IS-13-04, we excluded one outlier, nearly twice as old as the rest of the single-grain ages. In addition, we left out 1 order-of-magnitude older grain each from their two detrital (unreset) AHe samples from Neogene rocks; the remaining grains give a single age cluster for each sample (expressed as mean ages)

with a similar single-grain age dispersion as the other (reset) samples. The coordinates likely place the Neogene samples into the Pliocene Karanak Formation (IS-13-07: ~7.6 Ma AHe age) and the middle to upper Miocene Khingou or Tavildara Formations (IS-13-06: ~11.2 Ma). Given the ~25 °C/km paleo-geothermal gradient in the Tajik basin (Figure 3d), ≥ 3 km of overburden is needed to reset the AHe system in these detrital samples. The ~7.6-Ma mean age from the Pliocene (younger than ~5 Ma) sample is certainly from unreset apatites and the ~11.2-Ma mean age from the Miocene Formations (~20–5 Ma) likely too. The rare AHe ages from the Pamir span ~12–8 Ma (Rutte, Ratschbacher, Khan, et al., 2017), the more abundant Tian Shan ages ~26–2 Ma (median = ~7 Ma; Käßner et al., 2016); therefore, both areas are possible source regions for the detrital grain-age clusters in these samples.

Combining Chapman et al.'s (2017) and our data, what can be said about the evolution of the inversion of the Tajik basin? The age variability, the young ages, the difficulty with working with detrital apatites, and the paucity—but not absence—of parameters supporting the interpretation, that is, our track lengths and independent paleo-temperature information, demand a cautious interpretation of the entire thermochronologic database. Within uncertainty, Chapman et al.'s (2017) AFT ages from the Tajik basin and our study match, except for those from the Vakhsh anticlinorium, where theirs are half the age of our dates (Figures 3e and 5a). The age of sample 14-03, from an antiform farther east in the anticlinorium, overlaps within uncertainty with our Vakhsh anticlinorium ages. Their two oldest AFT ages are 15.6 ± 3.7 and 14.6 ± 2.9 Ma from the western Kafirnigan anticlinorium and the 12.2 ± 2.5 Ma age from the easternmost antiform of this anticlinorium overlaps with ours. Given the uncertainties of Chapman et al.'s (2017) ages—all including 12 Ma—and the consistency of our ages and their match with our ages from the Uzbek and Tajik Gissar, we conclude that none of their ages is older than ~12 Ma, thus consistent with our findings. The thermochronologic data thus indicate the simultaneous onset of inversion of the Tajik basin and the shortening in the Uzbek and Tajik Gissar (Käßner et al., 2016).

In addition, the oldest AHe ages (~12–8 Ma) of Chapman et al. (2017) match ours. The small age difference between the AFT and AHe ages imply that some thrusts show large displacements early in the inversion history (Figure 5a); in particular, this is the case for the Kafirnigan anticlinorium, for which Gaḡala et al. (2020) obtained the largest amount of shortening of any structure in the Tajik FTB. Furthermore, several thrust sheets, in particular those bounding the central depression of the Tajik basin and the Darvaz fault zone, have matching young AHe ages, suggesting reactivation. Given that growth strata indicate that also the eastern Tajik FTB started to shorten before ~11 Ma (Dedow et al., 2020; Gaḡala et al., 2020), the clustering of young AHe ages in the eastern Tajik FTB (Vakhsh anticlinorium to eastern Pamir margin) suggests that the young Tajik FTB reactivation is concentrated there. The scarcity of young reactivation in the Uzbek Gissar indicates that after regional synchronous initiation, shortening concentrated in the Tajik basin, where the evaporitic décollement facilitated thin-skinned deformation; this is particularly true for the eastern Tajik basin, where the widespread and thick salt has enabled related tectonics (e.g., Gaḡala et al., 2020; Nikolaev, 2002). The reactivation of the Tajik Gissar (with AHe ages as young as ~1.6 Ma) emphasizes its incorporation into the recent deformation field (Käßner et al., 2016; Schurr et al., 2014).

With six AFT dates and one AHe date, Jepson, Glorie, Konopelko, Gillespie, et al. (2018a) addressed the Cenozoic exhumation of the southern edge of the Garm massif. We recalculated their laser ablation-inductively coupled plasma-mass spectrometry AFT ages (Data Set S1 and Table S5), using a corrected single-grain data sheet provided by the authors, the decay constant $8.46 \times 10^{-17} \text{ a}^{-1}$ (instead of $7.03 \times 10^{-17} \text{ a}^{-1}$; Browne & Tuli, 2015; Holden & Hoffman, 2000), and a R-factor (half of the mean etchable spontaneous fission-track length) of 7.5 μm (instead of 7.0 μm ; Hasebe et al., 2004); this makes their ages younger. Five of their AFT ages are ~12.8–6.1 Ma, consistent with Käßner et al.'s (2016) ages that are not part of a fossil PAZ (their Figure 5). One sample (Gm-21) dated at ~18.3 Ma has shorter confined tracks than the younger samples, suggesting that it is part of a fossil PAZ, as most of Käßner et al.'s (2016) ages. Their single AHe sample (Gm-19) provided ~11.6- and 23.7-Ma ages for two aliquots, both older than the AFT age of the same sample. Based on one T-t model, Jepson, Glorie, Konopelko, Gillespie, et al. (2018a) contested the model of tectonic quiescence and burial between ~150 and 15 Ma based on seven T-t models in Käßner et al. (2016) and supported by another four models herein for the southwestern Tian Shan (Figures 4f and 4i). Jepson, Glorie, Konopelko, Gillespie, et al. (2018a) also reported a negative correlation between the ages and the uranium contents of their dated grains (their Figure 4). A possible explanation is either an

experimental artifact or—as argued by Jepson, Glorie, Konopelko, Gillespie, et al. (2018a)—radiation-enhanced annealing (Hendriks & Redfield, 2005). In the latter case, however, both the age and length reduction result at least in part from a nonthermal phenomenon, that is, radiation damage. This invalidates the T-t modeling results for Gm-21, which assume that track annealing is a thermal process (Ketcham et al., 2007). Little weight can therefore be attached to their initial ~25-Ma cooling event, contradicting the results of Käbner et al. (2016). In addition, Jepson, Glorie, Konopelko, Gillespie, et al. (2018a) overlooked that within <20 km of their sample—both at the northern and southern rims of the Garm massif, a transgressive section of Cretaceous-Neogene strata crops out north of the thin-skinned front of the Pamir (GRI, 1961–1964). The Oligocene-Neogene synorogenic rocks deposited in the Tajik basin and southern Tian Shan, which Klocke et al. (2017) measured to be ≥ 2.4 km thick in the remnant section on the southwestern edge of the Garm massif, must have caused burial. The sedimentologic data thus back up the burial interpretation of Käbner et al. (2016).

5.3. Coupling of Tajik-Basin Inversion and Tian Shan Shortening With the Pamir Hinterland

Based on the new data, the inversion of the Tajik basin and Uzbek Gissar started at ~13–12 Ma and was most active early on (~13–9 Ma); if the samples >12 Ma in the Uzbek Gissar are indeed from a fossil PAZ—the most likely interpretation—the onset is at ~12 Ma. Käbner et al. (2016) found the same evolution in the Tajik Gissar, now supported by the data of Jepson, Glorie, Konopelko, Gillespie, et al. (2018a). Thus, which event in the hinterland (Pamir plateau) evolution triggered the inversion of the foreland, that is, the Tajik basin and the southwestern Tian Shan? Given the time of inversion, the ~37- to 20-Ma thickening and the ~23–15 Ma, top-to-~N, foreland-directed gravitational collapse (by synconvergent crustal extension) of the Central Pamir plateau margin, cannot have been the trigger; it neither fits the kinematics nor the timing (see review in section 1; Hacker et al., 2017; Rutte, Ratschbacher, Khan, et al., 2017; Rutte, Ratschbacher, Schneider, et al., 2017; Stearns et al., 2013, 2015; Worthington et al., 2020). Instead, the argument of Kufner et al. (2016) that the northward advance of the western edge of the cratonic Indian lithosphere is currently forcing northward and westward rollback of cratonic Asian lithosphere (section 1) provides a compelling scenario; in particular, its onset at ~12–11 Ma is telling. We propose that the “hard” collision of the deep lithospheres (cratonic India with the Tajik-Tarim lithosphere) and the ensuing delamination and rollback of the lithosphere of the Tajik basin provided the trigger for its increased middle Miocene subsidence and ultimately the northward and westward advance of the Pamir-plateau crust into the Tajik depression (Schurr et al., 2014; Stübner, Ratschbacher, Rutte, et al., 2013; Stübner, Ratschbacher, Weise, et al., 2013), forming the asymmetric structure (Figure 2d) of the Tajik FTB. The synchronous foundering of the Pamir deep crust at ~14–11 Ma, documented in the xenoliths of the southeastern Pamir and related to the indentation process beneath the Pamir (Shaffer et al., 2017), provides an additional driving force by elevating the gravitational potential energy stored in the Pamir-plateau crust. The northward and westward progression of rollback of Asian lithosphere may have caused the young deepening of the southeastern (internal) Tajik-basin depocenter, the back-stepping of the upper Miocene-lower Pliocene synorogenic strata onto the North Pamir (Dedow et al., 2020; Klocke et al., 2017; Lyoskind et al., 1963), the young AHe ages, and the T-t models suggesting burial and rapid exhumation over the last few Myr in the internal Tajik FTB and the adjacent Pamir.

Our combined work on the amount and age of shortening of the Tajik basin and the southwestern Tian Shan (Käbner et al., 2016; Gągała et al., 2020; this study) and on the evolution of the Pamir (e.g., Kufner et al., 2016; Rutte, Ratschbacher, Khan, et al., 2017; Rutte, Ratschbacher, Schneider, et al., 2017; Hacker et al., 2017; Schurr et al., 2014; Shaffer et al., 2017; Stearns et al., 2013, 2015; Stübner, Ratschbacher, Rutte, et al., 2013; Stübner, Ratschbacher, Weise, et al., 2013; Worthington et al., 2020) may answer key questions about the evolution of the entire northwestern part of the India-Asia collision zone, in particular the central and western Tian Shan, in a unified way. Figure 6 summarizes the thermochronologic data on the time of moderate reheating, the time range or onset of modest cooling, and the onset of rapid cooling at well-studied localities in the western Tian Shan and the periphery of the Pamir. It also visualizes the tectonic scenario at the western edge of the India-Asia collision at ~12 Ma, when the advancing cratonic India met the Tajik-Tarim basin lithosphere (cratonic Asia), and delamination and rollback of Tajik-Tarim lithosphere commenced; the ~380-km northward progression of cratonic India beneath the Pamir is outlined by the present position of the northern edge of the Indian mantle lithosphere (see also Figure 2a; Kufner et al., 2016; Shaffer et al., 2017). Several studies (see citations in Figure 6 and below) have recognized that

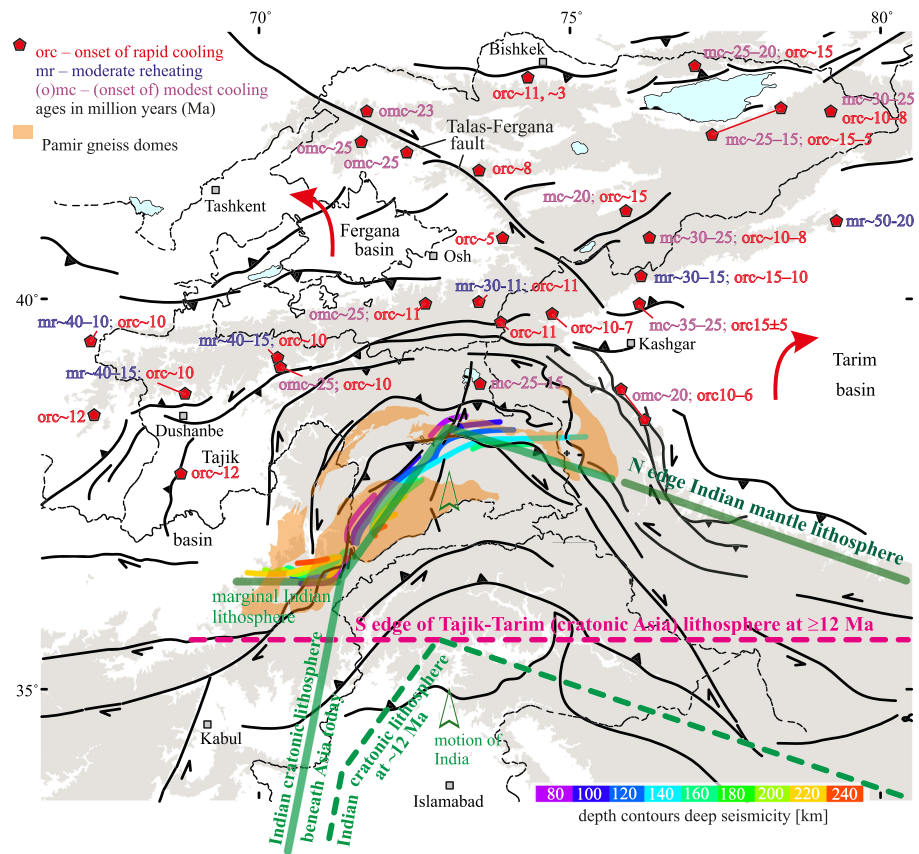


Figure 6. Tectonic overview map of the western corner of the India-Asia collision zone with main neotectonic structures drawn as black lines. Regions above 2.5-km sea level are shaded in gray, and Pamir gneiss domes are marked in orange. The colored contours mark the location and depth of the Pamir and Hindu Kush deep seismic zones (Kufner et al., 2017; Schneider et al., 2013; Sippl, Schurr, Tympel, et al., 2013, Sippl, Schurr, Yuan, et al., 2013). The northern edge of the Indian mantle lithosphere in western Tibet is from Zhao et al. (2010). The southern edge of cratonic Asia at ≥ 12 Ma is from the restoration of the arcuate Asian (Tajik-Tarim) lithospheric slab beneath the Pamir (Kufner et al., 2016; Schneider et al., 2013; Sippl, Schurr, Tympel, et al., 2013; Shaffer et al., 2017). The motion direction of India is from Molnar and Stock (2009). Northward movement of the northwestern corner of the subcrustal Indian cratonic lithosphere has driven rollback of the southern margin of Asia beneath the Pamir. The red pentagons and attached numbers give onset of rapid cooling (orc), time range of moderate reheating (mr), and time range or onset of modest cooling ((o)mc) at well-studied localities in the central and western Tian Shan and the periphery of the Pamir; data are from Bullen et al. (2003); (2013); (2013); Zhang et al. (2009); Amidon and Hynek (2010); Jolivet et al. (2010); Glorie et al. (2011); De Grave et al. (2012); Macaulay et al. (2013, 2014); Bande et al. (2015, 2017); Jia et al. (2015); and Jepson, Glorie, Konopolko, Gillespie, et al. (2018a), and references therein). The values are from thermochronologic studies and—given the uncertainties in age determination and thermal modeling—approximate. Regionally, they emphasize moderate reheating due to sediment burial along the southern margin of the Tian Shan and modest cooling due to low-strain shortening peaking at ~ 25 – 15 Ma in the more northern parts of the Tian Shan. This is followed by regional rapid cooling starting at ~ 12 Ma. The crustal thickening from ~ 37 to 20 Ma and the subsequent northward collapse of Pamir-plateau crust, manifested by crustal extension and the formation of the Pamir gneiss domes from ~ 20 to 15 Ma, may be responsible for the early low-strain event in the foreland. The collapse initiated crustal shortening across the North Pamir and subsidence due to sediment loading, expressed by moderate reheating, in the southern Tian Shan; farther north, it caused low-strain shortening, traced by modest cooling. The forceful coupling of deep India with deep Asia, marked by the indentation of the cratonic Indian lithosphere into the Tajik-Tarim (cratonic Asia) lithosphere beneath the Pamir has driven the inversion of the Tajik basin and the formation of the Tian Shan over the last ~ 12 Myr; it also imposed the opposite rotation of the relatively stable foreland blocks, that is, the anti-clockwise rotation of the Fergana basin and the clockwise rotation of the Tarim basin (marked by the curved arrows in the Tarim and Fergana basin).

Cenozoic reactivation of the Tian Shan commenced at low strain at ~ 30 – 20 Ma in isolated regions—in Figure 6, the time ranges of moderate reheating or modest cooling. Shortening has become significant over the last ~ 10 Myr—the onset of rapid cooling in Figure 6. Several of these studies

(e.g., Bande et al., 2017; De Grave et al., 2013; Glorie et al., 2010; Jolivet et al., 2010; Macaulay et al., 2014; Sobel, Chen, et al., 2006; Sobel, Oskin, et al., 2006; this study) suggested a period of rapid initial exhumation (~12–8 Ma).

In addition, T-t models discussed in some of these studies suggest moderate reheating between ~30 and 10 Ma over large regions of the southern Tian Shan; it was attributed to burial by Cenozoic strata when the Tajik basin extended into the southern Tian Shan. The area of modest cooling is farther north, beyond the ultimate northern reach of the Tajik basin. The two areas where T-t models may suggest modest cooling in the southern Tian Shan are from the interior of ranges close to major thrusts. The areal extent of the moderate reheating, modest cooling, and rapid cooling suggests regional drivers. Stress transfer from the Tarim block has been proposed as the impetus for the early Miocene exhumation in the central and eastern Tian Shan (e.g., Avouac et al., 1993; Yin et al., 1998). For the western Tian Shan, Pamir indentation was postulated as a tectonic driver (e.g., Bande et al., 2015; Burtman & Molnar, 1993; Sobel et al., 2013). However, these models do not explain why the Pamir and Tarim should drive deformation synchronously; that is, neither the Tarim nor the Pamir can be the single driver for the two-phase reactivation of the Tian Shan in the Cenozoic (e.g., Bande et al., 2017).

Two distinct events characterize the evolution of the Pamir-Tibet plateau; they can be traced best in the Pamir due to the exposure of Asian middle-lower crust and its deep seismic record. Following large-scale Paleogene (~37–20 Ma) crustal thickening, the South and Central Pamir and southern Tibet experienced orogen-wide synconvergent crustal extension (e.g., Hacker et al., 2017; Rutte, Ratschbacher, Schneider, et al., 2017; Stearns et al., 2013, 2015; Stübner, Ratschbacher, Weise, et al., 2013; Worthington et al., 2020). The switch from crustal shortening to extension at ~23–20 Ma was likely triggered by the slab breakoff of Greater India from cratonic India (see section 1). The crustal thickening and the subsequent, top-to-~N extensional collapse of the Pamir-plateau crust together with the bulk northward advance of the Pamir due to the India-Asia convergence initiated the foreland advance of the deformation front from the Central to the North Pamir, triggering the onset of crustal shortening across the North Pamir (Rutte, Ratschbacher, Khan, et al., 2017; Rutte, Ratschbacher, Schneider, et al., 2017; Li et al., 2019; Worthington et al., 2020) and—as we postulate here—north of it in the Tian Shan. Whereas the southern margin of the Tian Shan—the immediate foreland buttress of the North Pamir and depocenter of the Tajik basin—were loaded and subsided, the more distant Tian Shan was mildly shortened, with the modest structural reactivation indicated by enhanced cooling. The second event (~12–0 Ma) is related to the interpretation that northward advancing Indian lithosphere has been forcing delamination and rollback of Asia (Tajik-Tarim) lithosphere (Kufner et al., 2016, 2018), that is, the North Pamir and the basement of the Tajik basin, since ~12–11 Ma. Thus, it was the loading of the Tajik basin and the Tian Shan by the progressive crustal thickening and the ultimately the extensional collapse of the Pamir-plateau crust and thus the foreland-ward progression of the deformation front from the Central to the North Pamir that induced subsidence, burial and reheating, and shortening across their forelands at ~40–15 Ma. It was the indentation of deep India into deep Asia, that is, the forceful coupling of cratonic Indian and Asian lithospheres, which drove the inversion of the Tajik basin and the mountain building in the western and central Tian Shan over the last ~12 Myr. The latter also imposed the opposite rotation of the relative stable foreland blocks in the foreland of the western India-Asia collision zone, that is, the anticlockwise rotation of the Fergana basin and the clockwise rotation of the Tarim basin (Figure 6; e.g., Avouac et al., 1993; Thomas et al., 1993) with the Cenozoic Talas-Fergana fault zone as the boundary between these domains.

6. Conclusions

We addressed three major questions: (1) When were the Tajik basin and the southwestern Tian Shan inverted/reactivated to form the thin-skinned Tajik FTB and its thick-skinned southwestern Tian Shan foreland buttresses? (2) How did deformation progress in time? (3) How were inversion of the Tajik basin and shortening in the Tian Shan coupled with their hinterland, the Pamir-Tibet plateau? We report apatite fission-track (AFT) and zircon (ZHe) and apatite (U, Th)/He (AHe) thermochronologic data for clastic Lower Cretaceous Tajik-basin rocks, sampled along the major thrusts of the Tajik FTB, and

crystalline-basement and cover rocks of the southwestern Tian Shan (Uzbek and Tajik Gissar). Together, they date basin inversion and foreland reactivation.

The inversion of the Tajik basin and shortening of the southwestern Tian Shan commenced simultaneously at ~12 Ma. The shortening-driven erosion exhumed the rocks to ~2- to 3-km crustal depth within the first ~3–4 Myr, that is, most of the deformation was completed in the early history of inversion. Out-of-sequence reactivation is constrained by thermochronology to ~3–1 Ma and is concentrated in the Tajik basin, in particular its eastern, salt-floored part, which shows active salt tectonics; the rheologically weak salt likely facilitated long-lived shortening. Young ages (~6–1 Ma, AHe) also occur along the Darvaz fault zone in the easternmost part of the Tajik basin and in the Pamir hinterland (~10–6 Ma, AFT) adjacent to the margin of the Tajik basin. Furthermore, young AFT and AHe ages (~6.6–1.6 Ma) also characterize the actively eroding leading edge of the Pamir thrust system—the Vakhsh thrust—of the northeastern Tajik basin, where it narrows between the converging Tian Shan and Pamir.

The unreset AFT ages of the studied Neogene clastic rocks are the detrital signal of the major ~23- to 20-Ma thickening-erosion stage of the Central and South Pamir, they signify a short lag time between cooling and erosion in the hinterland and foreland deposition. The ages and temperature-time models of samples from a basement spur at the western edge of the southwestern Tian Shan indicate Jurassic-Cretaceous cooling, likely triggered by the Jurassic crustal extension along the southern margin of Asia, followed by burial and reheating by sediment loading roughly constrained between ~40 and 15 Ma.

We integrate the Cenozoic evolution of Pamir hinterland and the Tajik basin and southwestern Tian Shan foreland and discuss the causes of the two reactivation stages of the Tian Shan, reported in the literature and described herein. The first event is related the late Eocene-early Miocene evolution of the Pamir plateau, the pronounced crustal thickening followed by a switch from crustal shortening to extension during the top-to-~N collapse of the Pamir-plateau crust and the ensuing progression (foreland advance) of the deformation front from the Central Pamir to the North Pamir at ~23–15 Ma. The gravitational collapse of the South and Central Pamir, likely triggered by Indian slab break-off, induced the foreland advance of the deformation front, which in turn initiated crustal shortening across the North Pamir and subsidence in the southern and shortening in the more northerly western and central Tian Shan forelands. The second reactivation stage of the Tian Shan foreland is a result of the northward and westward rollback of Tajik (Asian) lithosphere, induced by its indentation by subcrustal Indian lithosphere since ~12–11 Myr. The rollback caused the depression of the foreland, that is, the southeastern edge of the Tajik-basin lithosphere, and ultimately the advance of the Pamir-plateau crust into the Tajik-basin depression, causing Tajik-basin inversion and shortening of the southwestern Tian Shan. We suggest that this deep lithospheric event, that is, the forceful coupling of deep India with deep Asia (Tajik-Tarim lithosphere), has driven the formation of the western and central Tian Shan over the last ~12 Ma. It was also this event that imposed the opposite rotation of the relatively stable blocks in the foreland of the western India-Asia collision zone, that is, the anti-clockwise rotation of the Fergana basin and the clockwise rotation of the Tarim basin.

Acknowledgments

Additional data are given in the supporting information and can be downloaded from <https://opara.zih.tu-dresden.de/xmlui/handle/123456789/1683?locale-attribute=en>. DFG bundle TIPAGE (PAK 443), DFG projects RA 442/37 and 40, project CLIENT II - CaTeNA of the German Federal Ministry of Education and Research (support code 03G0878B), and a research grant from TOTAL funded this work. S. A. received scholarships from Damascus University, and the State of Saxony. DAAD supported M. N. and L. R. A. S. acknowledges an A. v. Humboldt fellowship and J. K. one from The University of Azad Jammu and Kashmir, Muzaffarabad. We acknowledge reviews by J. Chapman, G. Jepson, and an anonymous referee. Work in Tajikistan would have been impossible without the support of the Tajik Academy of Sciences, in particular V. Minaev. Research in Uzbekistan was made possible by R. Mirkamalov and his colleagues from the Uzbek Academy of Sciences. We dedicate this paper to N. Rajabov (Tajik Academy of Sciences) for guiding us through the Tajik basin.

References

- Abdullaev, K. A., & Rzhovsky, Y. S. (1973). *Lower Cretaceous paleomagnetism of the Tajik basin*, (p. 104). Tashkent, Uzbekistan: Donish. (in Russian)
- Amidon, W. H., & Hynek, S. A. (2010). Exhumational history of the north Central Pamir. *Tectonics*, 29, TC5015. <https://doi.org/10.1029/2009TC002589>
- Avouac, J. P., Tapponnier, P., Bai, M., You, H., & Wang, G. (1993). Active thrusting and folding along the northern Tien Shan and late Cenozoic rotation of the Tarim relative to Dzungaria and Kazakhstan. *Journal of Geophysical Research*, 98, 6755–6804. <https://doi.org/10.1029/92JB01963>
- Babaev, A. M. (1975). *Recent Tectonic of the zone of orogenesis of the Gissar-Alia and Tajik Depression*, (p. 149). Dushanbe, Tajikistan: Donish. (in Russian)
- Bande, A., Sobel, E. R., Mikolaichuk, A., Schmidt, A., & Stockli, D. F. (2017). Exhumation history of the western Kyrgyz Tien Shan: Implications for intra-montane basin formation. *Tectonics*, 36, 163–180. <https://doi.org/10.1002/2017TC004284>
- Bande, A., Sobel, E. R., Mikolaichuk, A., & Torres Acosta, V. (2015). Talas–Fergana Fault Cenozoic timing of deformation and its relation to Pamir indentation. In M.-F. Brunet, T. McCann, & E. R. Sobel (Eds.), *Geological Evolution of Central Asian Basins and the Western Tien Shan Range*. (Vol. 427, pp. 295–311). London: Geol. Soc., London, Spec. Publ. <https://doi.org/10.1144/SP427.1>
- Barker, C. E., & Goldstein, R. H. (1990). Fluid inclusion technique for determining maximum temperature in calcite and its comparison to the vitrinite reflectance geothermometers. *Geology*, 18, 1003–1006.
- Bazhenov, M. L., Perroud, H., Chauvin, A., Burtman, V. S., & Thomas, J.-C. (1994). Paleomagnetism of cretaceous red beds from Tadzhikistan and Cenozoic deformation due to India–Eurasia collision. *Earth and Planetary Science Letters*, 124, 1–18. [https://doi.org/10.1016/0012-821X\(94\)00072-7](https://doi.org/10.1016/0012-821X(94)00072-7)

- Bekker, Y. A. (1996). Tectonics of the Afghan-Tajik basin. *Geotektonika*, 1, 76–82. (in Russian)
- Bourgeois, O., Cobbold, P. R., Rouby, D., & Thomas, J.-C. (1997). Least squares restoration of Tertiary thrust sheets in map view, Tajik depression, central Asia. *Journal of Geophysical Research*, 102, 27,553–27,573.
- Browne, E., & Tuli, J. (2015). Nuclear data sheet for A = 238*. *Nuclear Data Sheets*, 127, 191–332.
- Brunet, M.-F., Ersho, A. V., Korotaev, M. V., Melikhov, V. N., Barrier, E., Mordvintsev, D. O., & Sidorova, I. P. (2017). Late Paleozoic and Mesozoic evolution of the Amu Darya Basin (Turkmenistan, Uzbekistan). In M.-F. Brunet, T. McCann, & E. R. Sobel (Eds.), *Geological Evolution of Central Asian Basins and the Western Tien Shan Range*. Geological Society, (Vol. 427, pp. 89–144). London: Special Publications. <https://doi.org/10.1144/SP427.18>
- Bullen, M. E., Burbank, D. W., & Garver, J. I. (2003). Building the Northern Tien Shan: Integrated thermal, structural, and topographic constraints. *Journal of Geology*, 111(2), 149–165. <https://doi.org/10.1086/345840>
- Burmakin, A. V., Starshinin, D. A., & Likhachev, V. I. (1961). Geological map of the USSR of 1: 200 000 scales, *Sheet J-42-XI*, Russ. Geol. Res. Inst., Nedra, Moscow.
- Burtman, V. S. (2000). Cenozoic crustal shortening between the Pamir and Tien Shan and a reconstruction of the Pamir-Tien Shan transition zone for the Cretaceous and Palaeogene. *Tectonophysics*, 319, 69–92.
- Burtman, V. S., & Molnar, P. (1993). Geological and geophysical evidence for deep subduction of continental crust beneath the Pamir. *Special Papers - Geological Society of America*, 281, 1–76. <https://doi.org/10.1130/SPE281-p1>
- Carrapa, B., DeCelles, P. G., Wang, X., Clementz, M. T., Mancin, N., Stoica, M., et al. (2015). Tectono-climatic implications of Eocene Paratethys regression in the Tajik basin of Central Asia. *Earth and Planetary Science Letters*, 424, 168–178. <https://doi.org/10.1016/j.epsl.2015.05.034>
- Chapman, J. B., Carrapa, B., Ballato, P., DeCelles, P. G., Worthington, J., Oimahmadov, I., et al. (2017). Intracontinental subduction beneath the Pamir Mountains: Constraints from thermokinematic modeling of shortening in the Tajik fold-and-thrust belt. *Geological Society of America Bulletin*, 129, 1450–1471. <https://doi.org/10.1130/B31730.1>
- Chapman, J. B., Carrapa, B., DeCelles, P. G., Worthington, J., Mancin, N., Cobianchi, M., et al. (2019). The Tajik basin: A composite record of sedimentary basin evolution in response to tectonics in the Pamir. *Basin Research*, bre.12381. <https://doi.org/10.1111/bre.12381>
- De Grave, J., Glorie, S., Buslov, M. M., Stockli, D. F., McWilliams, M. O., Batalev, V. Y., & Van den haute, P. (2013). Thermo-tectonic history of the Issyk Kul basement (Kyrgyz Northern Tien Shan, Central Asia). *Gondwana Research*, 23(3), 998–1020. <https://doi.org/10.1016/j.gr.2012.06.014>
- De Grave, J., Glorie, S., Ryabinin, A., Zhimulev, F., Buslov, M. M., Izmer, A., et al. (2012). Late Paleozoic and Meso-Cenozoic tectonic evolution of the Southern Kyrgyz Tien Shan: Constraints from multi-method thermochronology in the Trans-Alai, Turkestan-Alai section and the southeastern Ferghana Basin. *Journal of Asian Earth Sciences*, 40, 149–168. <https://doi.org/10.1016/j.jseas.2011.04.019>
- Dedow, R., Franz, M., Szulc, A., Schneider, J. W., Brückner, J., Ratschbacher, L., et al. (2020). Tajik Basin and Southwestern Tien Shan, Northwestern India-Asia Collision Zone: 3. Pre- to Syn-orogenic Retro-foreland Basin Evolution in the Eastern Tajik Depression and Linkage to the Pamir Hinterland. *tectonics*, 39, e2019TC005874. <https://doi.org/10.1029/2019TC005874>
- Doeblich, J. L., & Wahl R. R. (Compilers) (2006). Geological and mineral resource map of Afghanistan; *Version 2*. U.S. Geol. Surv. Open File Rep., 2006–1038.
- Farley, K. A., & Stockli, D. F. (2002). (U-Th)/He dating of phosphates: Apatite, monazite, and xenotime. In B. Kohn, & P. K. Zeitler (Eds.), *Phosphates—Geochemical, geobiological and material importance* (Vol. 48, pp. 557–577). Chantilly, VA: Reviews in Mineralogy and Geochemistry, Mineralogical Society of America. <https://doi.org/10.2138/rmg.2002.48.15>
- Farley, K. A., Wolf, R. A., & Silver, L. T. (1996). The effects of long alpha-stopping distances on (U-Th)/He dates. *Geochimica et Cosmochimica Acta*, 60, 4223–4230.
- Fürsich, F., Brunet, M.-F., Auxietre, J.-L., & Munsch, H. (2015). Lower–Middle Jurassic facies patterns in the NW Afghan–Tajik Basin of southern Uzbekistan and their geodynamic context. In M.-F. Brunet, T. McCann, & E. R. Sobel (Eds.), *Geological Evolution of Central Asian Basins and the Western Tien Shan Range* (Vol. 427, pp. 357–409). London: Geol. Soc., London, Spec. Publ. <http://doi.org/10.1144/SP427.9>
- Gagała, L. (2014). Structural geometry and kinematics of the Tajik depression, Central Asia: Neogene basin inversion in front of the Pamir salient (Doctoral dissertation). Retrieved from <http://swbplus.bsz-bw.de/bsz420285989inh.htm>. Technischen Universität Bergakademie Freiberg, Germany.
- Gagała, L., Ratschbacher, L., Ringenbach, J.-C., Kufner, S.-K., Schurr, B., Dedow, R. et al. (2020). Tajik basin and southwestern Tien Shan, northwestern India-Asia collision zone: 1. Structure, kinematics, and salt-tectonics in the Tajik fold-and-thrust belt of the western foreland of the Pamir. *Tectonics*, 39, part 1 of this paper series.
- Galbraith, R. F. (1990). The radial plot: Graphical assessment of spread in ages. *Nuclear Tracks and Radiation Measurements*, 17, 207–214. [https://doi.org/10.1016/1359-0189\(90\)90036-W](https://doi.org/10.1016/1359-0189(90)90036-W)
- Glorie, S., De Grave, J., Buslov, M. M., Elburg, M. A., Stockli, D. F., & Gerdes, A. (2010). Multi-method chronometric constraints on the evolution of the northern Kyrgyz Tien Shan granitoids (Central Asian Orogenic Belt): from emplacement to exhumation. *Journal of Asian Earth Sciences*, 38(3-4), 131–146. <https://doi.org/10.1016/j.jseas.2009.12.009>
- Glorie, S., De Grave, J., Buslov, M. M., Zhimulev, F., Stockli, D. F., Batalev, V. Y., et al. (2011). Tectonic history of the Kyrgyz South Tien Shan (Atbashi-Inylchek) suture zone: The role of inherited structures during deformation propagation. *Tectonics*, 30, TC6016. <https://doi.org/10.1029/2011TC002949>
- Green, P. F., Duddy, I. R., Gleadow, A. J. W., Tingate, P. R., & Laslett, G. M. (1986). Thermal annealing of fission tracks in apatite: 1. A qualitative description. *Chemical Geology (Isotope Geoscience Section)*, 59, 237–253.
- Hacker, B. R., Ratschbacher, L., Rutte, D., Stearns, M. A., Malz, N., Stübner, K., et al. (2017). Building the Pamir-Tibet Plateau—Crustal stacking, extensional collapse, and lateral extrusion in the Central Pamir: 3. Thermobarometry and Petrochronology of deep Asian crust. *Tectonics*, 36, 1743–1766. <https://doi.org/10.1002/2017TC004488>
- Hasebe, N., Barbarand, J., Jarvis, K., Carter, A., & Hurford, A. J. (2004). Apatite fission-track chronometry using laser ablation ICP-MS. *Chemical Geology*, 207, 135–145.
- Hendriks, B. W. H., & Redfield, T. F. (2005). Apatite fission track and (U-Th)/He data from Fennoscandia: An example of underestimation of fission track annealing in apatite. *Earth and Planetary Science Letters*, 236, 443–458.
- Holden, N. E., & Hoffman, D. C. (2000). Spontaneous fission half-lives for ground-state nuclides (technical report). *Pure and Applied Chemistry*, 72, 1525–1562.

- Ischuk, A., Bendick, R., Rybin, A., Molnar, P., Khan, S. F., Kuzikov, S., et al. (2013). Kinematics of the Pamir and Hindu Kush regions from GPS geodesy. *Journal of Geophysical Research, Solid Earth*, *118*, 2408–2416. <https://doi.org/10.1002/jgrb.50185>
- Jepson, G., Glorie, S., Konopelko, D., Gillespie, J., Danišik, M., Evans, N. J., et al. (2018a). Thermochronological insights into the structural contact between the Tian Shan and Pamirs, Tajikistan. *Terra Nova*, *30*, 95–104. <https://doi.org/10.1111/ter.12313>
- Jepson, G., Glorie, S., Konopelko, D., Gillespie, J., Danišik, M., Mirkamalov, R., et al. (2018b). Low-temperature thermochronology of the Chatkal-Kurama terrane (Uzbekistan-Tajikistan): Insights into the Meso-Cenozoic thermal history of the western Tian Shan. *Tectonics*, *37*, 3954–3969. <https://doi.org/10.1029/2017TC004878>
- Jepson, G., Glorie, S., Konopelko, D., Mirkamalov, R., Danišik, M., & Collins, A. S. (2018). The low-temperature thermo-tectonic evolution of the western Tian Shan, Uzbekistan. *Gondwana Research*, *64*, 122–136. <https://doi.org/10.1016/j.gr.2018.08.003>
- Jia, Y., Fu, B., Jolivet, M., & Zhang, S. (2015). Cenozoic tectono-geomorphological growth of the SW Chinese Tian Shan: Insight from AFT and detrital zircon U-Pb data. *Journal of Asian Earth Sciences*, *111*, 395–413. <https://doi.org/10.1016/j.jseas.2015.06.23>
- Jolivet, M., Dominguez, S., Charreau, J., Chen, Y., Li, Y., & Wang, Q. (2010). Mesozoic and Cenozoic tectonic history of the central Chinese Tian Shan: Reactivated tectonic structures and active deformation. *Tectonics*, *29*, TC6019. <https://doi.org/10.1029/2010TC002712>
- Käbner, A., Ratschbacher, L., Jonckheere, R., Enkelmann, E., Khan, J., Sonntag, B.-L., et al. (2016). Cenozoic intracontinental deformation and exhumation at the northwestern tip of the India-Asia collision–southwestern Tian Shan, Tajikistan, and Kyrgyzstan. *Tectonics*, *35*, 2171–2194. <https://doi.org/10.1002/2015TC003897>
- Käbner, A., Ratschbacher, L., Pfänder, J. A., Hacker, B. R., Zack, G., Sonntag, B.-L., et al. (2017). Proterozoic-Mesozoic history of the central Asian Orogenic Belt in the Tajik and southwestern Kyrgyz Tian Shan: U-Pb, ⁴⁰Ar/³⁹Ar, fission-track geochronology, and geochemistry of granitoids. *Geological Society of America Bulletin*, *129*, 281–303. <https://doi.org/10.1130/B31466.1>
- Ketcham, R. A. (2005). Forward and inverse modeling of low-temperature thermochronometry data. In P. W. Reiners, & T. A. Ehlers (Eds.), *Low Temperature Thermochronology: Techniques, Interpretations and Applications*, Reviews in Mineralogy and Geochemistry, (Vol. 58, pp. 275–314). Chantilly, VA: Reviews in Mineralogy and Geochemistry, Mineralogical Society of America. <https://doi.org/10.2138/rmg.2005.58.11>
- Ketcham, R. A., Carter, A., Donelick, R. A., Barbarand, J., & Hurford, A. J. (2007). Improved measurement of fission-track annealing in apatite using c-axis projection. *American Mineralogist*, *92*, 789–798.
- Klocke, M., Voigt, T., Kley, J., Pfeifer, S., Rocktäschel, T., Keil, S., & Gaupp, R. (2017). Cenozoic evolution of the Pamir and Tien Shan mountains reflected in syntectonic deposits of the Tajik Basin. In M.-F. Brunet, T. McCann, & E. R. Sobel (Eds.), *Geological evolution of Central Asian Basins and the Western Tien Shan Range*, (Vol. 427, pp. 523–564). London: Geological Society, Special Publications (Vol. <https://doi.org/10.1144/SP427.7>
- Kufner, S.-K., Schurr, B., Haberland, C., Zhang, Y., Saul, J., Ischuk, A., & Oimahmadov, I. (2017). Zooming into the Hindu Kush slab break-off: A rare glimpse on the terminal stage of subduction. *Earth and Planetary Science Letters*, *461*, 127–140. <https://doi.org/10.1016/j.epsl.2016.12.043>
- Kufner, S.-K., Schurr, B., Ratschbacher, L., Murodkulov, S., Abdulhameed, S., Ischuk, A., et al. (2018). Seismotectonics of the Tajik basin and surrounding mountain ranges. *Tectonics*, *37*(8), 2404–2424. <https://doi.org/10.1029/2017TC004812>
- Kufner, S.-K., Schurr, B., Sippl, C., Yuan, X., Ratschbacher, L., Ischuk, A., et al. (2016). Deep India meets deep Asia: Lithospheric indentation, delamination and break-off under Pamir and Hindu Kush (Central Asia). *Earth and Planetary Science Letters*, *435*, 171–184.
- Leith, W., & Simpson, D. W. (1986). Seismic domains within the Gissar-Kokshal seismic zone, Soviet Central Asia. *Journal of Geophysical Research*, *91*(B1), 689–699.
- Li, T., Chen, Z., Chen, J., Thompson Jobe, J. A., Burbank, D. W., Li, Z., et al. (2019). Along-strike and down-dip segmentation of the Pamir frontal thrust and its association with the 1985 Mw 6.9 Wuqia earthquake. *Journal of Geophysical Research - Solid Earth*, *124*, 9890–9919. <https://doi.org/10.1029/2019JB017319>
- Lyoskind, S. Y., Novikova, L. A., & Yakusheva, V. M. (1964). *Geological map of the USSR of 1: 200 000 scales, Sheet J-42-XVI*. Nedra, Moscow: Russ. Geol. Res. Inst.
- Lyoskind, S. Y., Novikova, L. A., & Dolgonos, L. G. (1963). *Geological map of the USSR of 1: 200 000 scales, Sheet J-42-XVII*, Russ. Geol. Res. Inst., Nedra, Moscow.
- Macaulay, E. A., Sobel, E. R., Mikolaichuk, A., Kohn, B., & Stuart, F. (2014). Cenozoic deformation and exhumation history of the Central Kyrgyz Tien Shan. *Tectonics*, *33*, 135–165. <https://doi.org/10.1002/2013TC003376>
- Macaulay, E. A., Sobel, E. R., Mikolaichuk, A., Landgraf, A., Kohn, B., & Stuart, F. (2013). Thermochronologic insight into late Cenozoic deformation in the basement-cored Terskey Range, Kyrgyz Tien Shan. *Tectonics*, *32*, 487–500. <https://doi.org/10.1002/tect.20040>
- Mechie, J., Yuan, X., Schurr, B., Schneider, F., Sippl, C., Ratschbacher, L., et al. (2012). Crustal and uppermost mantle velocity structure along a profile across the Pamir and southern Tien Shan as derived from project TIPAGE wide-angle seismic data. *Geophysical Journal International*, *188*(2), 385–407. <https://doi.org/10.1111/j.1365-246X.2011.05278.x>
- Molnar, P., & Stock, J. M. (2009). Slowing of India's convergence with Eurasia since 20 Ma and its implications for Tibetan mantle dynamics. *Tectonics*, *28*(3), TC3001. <https://doi.org/10.1029/2008TC002271>
- Mordvintsev, D., Barrier, E., Brunet, M.-F., Blanpied, C., & Sidorova, I. (2017). Structure and evolution of the Bukhara-Khiva region during the Mesozoic: The northern margin of the Amu-Darya Basin (southern Uzbekistan). In M.-F. Brunet, M.-F. T. McCann, & E. R. Sobel (Eds.), *Geological evolution of Central Asian Basins and the Western Tien Shan Range*. Geological Society, (Vol. 427, pp. 145–174). London: Special Publications. <https://doi.org/10.1144/SP427.16>
- Nikolaev, V. G. (2002). Afghan-Tajik depression: Architecture of sedimentary cover and evolution. *Russian Journal of Earth Sciences*, *4*(6), 399–421.
- Pavlis, T. L., Hamburger, M. W., & Pavlis, G. L. (1997). Erosional processes as a control on the structural evolution of an actively deforming fold and thrust belt: An example from the Pamir-Tien Shan region, central Asia. *Tectonics*, *16*, 810–822.
- Pegler, G., & Das, S. (1998). An enhanced image of the Pamir Hindu Kush seismic zone from relocated earthquake hypocenters. *Geophysical Journal International*, *134*, 573–595. <https://doi.org/10.1046/j.1365-246x.1998.00582.x>
- Perry, M., Kakar, N., Ischuk, A., Metzger, S., Bendick, R., Molnar, P., & Mohadjer, S. (2019). Little geodetic evidence for localized Indian subduction in the Pamir-Hindu Kush of Central Asia. *Geophysical Research Letters*, *46*, 109–118. <https://doi.org/10.1029/2018GL080065>
- Pozzi, J.-P., & Feinberg, H. (1991). Paleomagnetism in the Tajikistan: Continental shortening of European margin in the Pamirs during Indian Eurasian collision. *Earth and Planetary Science Letters*, *103*, 365–378.
- Ratschbacher, L., Frisch, W., Linzer, H.-G., & Merle, O. (1991). Lateral extrusion in the eastern Alps, part 2: Structural analysis. *Tectonics*, *10*(2), 257–271. <https://doi.org/10.1029/90TC02623>
- Reiners, P. W., Spell, T. L., Nicolescu, S., & Zanetti, K. A. (2004). Zircon (U, Th)/He thermometry: He diffusion and comparisons with ⁴⁰Ar/³⁹Ar dating. *Geochimica et Cosmochimica Acta*, *68*, 1857–1887.

- Replumaz, A., Negredo, A. M., Guillot, S., & Villaseñor, S. (2010). Multiple episodes of continental subduction during India/Asia convergence: Insight from seismic tomography and tectonic reconstruction. *Tectonophysics*, *483*(1), 125–134. <https://doi.org/10.1016/j.tecto.2009.10.007>
- Rey, P. F., Teyssier, C., & Whitney, D. L. (2010). Limit of channel flow in orogenic plateaux. *Lithosphere*, *2*(5), 328–332. <https://doi.org/10.1130/L114.1>
- Robinson, A. C., Yin, A., Manning, C. E., Harrison, T. M., Zhang, S.-H., & Wang, X.-F. (2004). Tectonic evolution of the northeastern Pamir: Constraints from the northern portion of the Cenozoic Kongur Shan extensional system. *Geological Society of America Bulletin*, *116*, 953–974. <https://doi.org/10.1130/B25375.1>
- Robinson, A. C., Yin, A., Manning, C. E., Harrison, T. M., Zhang, S.-H., & Wang, X.-F. (2007). Cenozoic evolution of the eastern Pamir: Implications for strain-accommodation mechanisms at the western end of the Himalayan-Tibetan orogen. *Geological Society of America Bulletin*, *119*, 882–896. <https://doi.org/10.1130/B25981.1>
- Rubanov, D. A., Puniklenko, I. A., Rubanov, A. A., & Alfyorov, G. Y. (1963). Geological map of the USSR of 1: 200 000 scales, Sheet J-42-XIV, Russ. Geol. Res. Inst., Nedra, Moscow.
- Ruleman, C. A., Crone, A. J., Machette, M. N., Haller, K. M., & Rukstales, K. S. (2007). Map and database of probable and possible Quaternary faults in Afghanistan, *U.S. Geological Survey Open-File Report 2007-1103*, 39 p., 1 plate.
- Rutte, D., Ratschbacher, L., Khan, J., Stübner, K., Hacker, B. R., Stearns, M. A., et al. (2017). Building the Pamir-Tibet Plateau—Crustal stacking, extensional collapse, and lateral extrusion in the central Pamir: 2. Timing and rates. *Tectonics*, *36*(3), 385–419. <https://doi.org/10.1002/TC004294>
- Rutte, D., Ratschbacher, L., Schneider, S., Stübner, K., Stearns, M. A., Gulzar, M. A., & Hacker, B. R. (2017). Building the Pamir-Tibet Plateau—Crustal stacking, extensional collapse, and lateral extrusion in the central Pamir: 1. Geometry and kinematics. *Tectonics*, *36*, 342–384. <https://doi.org/10.1002/2016TC004293>
- Sass, P., Ritter, O., Ratschbacher, L., Tjampel, J., Matiukov, V. E., Rybin, A. K., & Batalev, V. Y. (2014). Resistivity structure underneath the Pamir and Southern Tian Shan. *Geophysical Journal International*, *198*(1), 564–579. <https://doi.org/10.1093/gji/ggu146>
- Schneider, F. M., Yuan, X., Schurr, B., Mechie, J., Sippl, C., Haberland, C., et al. (2013). Seismic imaging of subducting continental lower crust beneath the Pamir. *Earth and Planetary Science Letters*, *375*, 101–112. <https://doi.org/10.1016/j.epsl.2013.05.015>
- Schneider, F. M., Yuan, X., Schurr, B., Mechie, J., Sippl, C., Kufner, S.-K., et al. (2019). The crust in the Pamir: Insights from receiver functions. *Journal of Geophysical Research - Solid Earth*, *124*(8), 9313–9331. <https://doi.org/10.1029/2019JB017765>
- Schurr, B., Ratschbacher, L., Sippl, C., Gloaguen, R., Yuan, X., & Mechie, J. (2014). Seismotectonics of the Pamir. *Tectonics*, *33*(8), 1501–1518. <https://doi.org/10.1002/2014TC003576>
- Shaffer, M., Hacker, B. R., Ratschbacher, L., & Kylander-Clark, A. R. C. (2017). Recycling of continental crust captured in xenoliths: A history of founding triggered by the collision of India and Asia beneath the Pamir. *Tectonics*, *36*, 1913–1933. <https://doi.org/10.1002/2017TC004704>
- Sippl, C., Ratschbacher, L., Schurr, B., Krumbiegel, C., Rui, H., Pingren, L., & Abdybaeva, U. (2014). The 2008 Nura earthquake sequence at the Pamir-Tian Shan collision zone, southern Kyrgyzstan. *Tectonics*, *33*(12), 2382–2399. <https://doi.org/10.1002/2014TC003705>
- Sippl, C., Schurr, B., Tjampel, J., Angiboust, S., Mechie, J., Yuan, X., et al. (2013). Deep burial of Asian continental crust beneath the Pamir imaged with local earthquake tomography. *Earth and Planetary Science Letters*, *384*, 165–177. <https://doi.org/10.1016/j.epsl.2016.12.043>
- Sippl, C., Schurr, B., Yuan, X., Mechie, J., Schneider, F. M., Gadoev, M., et al. (2013). Geometry of the Pamir-Hindu Kush intermediate-depth earthquake zone from local seismic data. *Journal of Geophysical Research - Solid Earth*, *118*(4), 1438–1457. <https://doi.org/10.1002/jgrb.50128>
- Sobel, E., Chen, J., Schoenbohm, L., Thiede, R., Stockli, D., Sudo, M., & Strecker, M. (2013). Oceanic-style subduction controls late Cenozoic deformation of the Northern Pamir orogen. *Earth and Planetary Science Letters*, *363*, 204–218.
- Sobel, E. R., Chen, J., & Heermance, R. V. (2006). Late Oligocene–Early Miocene initiation of shortening in the Southwestern Chinese Tian Shan: Implications for Neogene shortening rate variations. *Earth and Planetary Science Letters*, *247*, 70–81. <https://doi.org/10.1016/j.epsl.2006.03.048>
- Sobel, E. R., Oskin, M., Burbank, D., & Mikolaichuk, A. (2006). Exhumation of basement-cored uplifts: Example of the Kyrgyz Range quantified with apatite fission-track thermochronology. *Tectonics*, *25*, TC2008. <https://doi.org/10.1029/2005TC001809>
- Stearns, M. A., Hacker, B. R., Ratschbacher, L., Lee, J., Cottle, J. M., & Kylander-Clark, A. R. C. (2013). Synchronous Oligocene–Miocene metamorphism of the Pamir and the north Himalaya driven by plate-scale dynamics. *Geology*, *41*, 1071–1074. <https://doi.org/10.1130/GE34451.1>
- Stearns, M. A., Hacker, B. R., Ratschbacher, L., Rutte, D., & Kylander-Clark, A. R. C. (2015). Titanite petrochronology of the Pamir gneiss domes: Implications for mid–deep crust exhumation and titanite closure to Pb and Zr diffusion. *Tectonics*, *34*, 784–802. <https://doi.org/10.1002/2014TC003774>
- Stübner, K., Ratschbacher, L., Rutte, D., Stanek, K., Minaev, V., Wiesinger, R., Gloaguen R, Project TIPAGE members (2013). The giant Shakh dara migmatitic gneiss dome, Pamir, India-Asia collision zone. 1: Geometry and kinematics. *Tectonics*, *32*, 948–979. <https://doi.org/10.1002/tect.20057>, n/a.
- Stübner, K., Ratschbacher, L., Weise, C., Chow, J., Hofmann, J., Khan, J., et al., & Project TIPAGE members (2013). The giant Shakh dara migmatitic gneiss dome, Pamir, India-Asia collision zone: 2. Timing of dome formation. *Tectonics*, *32*, 1404–1431. <https://doi.org/10.1002/tect.20059>
- Sweeney, J. J., & Burnham, A. K. (1990). Evaluation of a simple model of vitrinite reflectance based on chemical kinetics. *AAPG Bulletin*, *74*, 1559–1570.
- Taylor, G. H., Teichmüller, M., Davis, A., Diessel, C. F. K., Littke, R., & Robert, P. (1998). *Organic petrology*, (p. 704). Berlin & Stuttgart: Gebrüder Borntraeger.
- Thomas, J.-C., Chauvin, A., Gapais, D., Bazhenov, M. L., Perroud, H., Cobbold, P. R., & Burtman, V. S. (1994). Paleomagnetic evidence for Cenozoic block rotations in the Tadjik depression (Central Asia). *Journal of Geophysical Research*, *99*, 15,141–15,160.
- Thomas, J. C., Cobbold, P. R., Wright, A., & Gapais, D. (1996). Cenozoic tectonics of the Tadjik depression, Central Asia. In A. Yin, & T. M. Harrison (Eds.), *The Tectonic Evolution of Asia*, (pp. 191–210). Cambridge: Cambridge University Press.
- Thomas, J. C., Gapais, D., Cobbold, P. R., Meyer, V., & Burtman, V. S. (1994). Tertiary kinematics of the Tadjik Depression (central Asia): Inferences from fault and fold patterns. In F. Roure, N. E., V. S. Shein, & I. Skvortsov (Eds.), *Geodynamic evolution of sedimentary basins, International Symposium* (pp. 171–180). Paris: Editions Technip.

- Thomas, J. C., Perroud, H., Cobbold, P. R., Burtman, V. S., Chauvin, A., Perroud, H., et al. (1993). A paleomagnetic study of Tertiary formations from the Kyrgyz Tien-Shan and its tectonic implications. *Journal of Geophysical Research*, *98*, 9571–9589. <https://doi.org/10.1029/92JB02912>
- Vlasov, N. G., Dyakov, Y. A., & Cherev, E. S. (1991). Geological map of the Tajik SSR and adjacent territories, 1:500,000, Vsesojuznoi Geol. Inst. Leningrad, Saint Petersburg.
- Wauschkuhn, B., Jonckheere, R., & Ratschbacher, L. (2015). The KTB apatite fission-track profiles: Building on a firm foundation? *Geochimica et Cosmochimica Acta*, *167*, 27–62. <https://doi.org/10.1016/j.gca.2015.06.015>
- Worthington, J. R., Ratschbacher, L., Stübner, K., Khan, J., Malz, N., Schneider, S., et al. (2020). The Alichur dome, South Pamir, western India–Asia collisional zone: Detailing the Neogene Shakh dara–Alichur syn-collisional gneiss-dome complex and connection to lithospheric processes. *Tectonics*, *39*, e2019TC005735. <https://doi.org/10.1029/2019TC005735>
- Yin, A., Nie, S., Craig, P., Harrison, T. M., Ryerson, F. Y., Xianglin, Q., & Geng, Y. (1998). Late Cenozoic tectonic evolution of the southern Chinese Tian Shan. *Tectonics*, *17*(1), 1–27. <https://doi.org/10.1029/97TC03140>
- Zhang, Z. Y., Zhu, W. B., Shu, L. S., Wan, J. L., Yang, W., Su, J. B., & Zheng, B. H. (2009). Apatite fission track thermochronology of the Precambrian Aksu blueschist, NW China: Implications for thermo–tectonic evolution of the north Tarim basement. *Gondwana Research*, *16*, 182–188.
- Zhao, J., Yuan, X., Liu, H., Kumar, P., Pei, S., Kind, R., et al. (2010). The boundary between the Indian and Asian tectonic plates below Tibet. *Proceedings of the National Academy of Sciences*. <https://doi.org/10.1073/pnas.1001921107>
- Zubovich, A., Schöne, T., Metzger, S., Mosienko, O., Mukhamediev, S., Sharshabaev, A., & Zech, C. (2016). Tectonic interaction between the Pamir and Tien Shan observed by GPS. *Tectonics*, *35*(2), 283–292. <https://doi.org/10.1002/2015TC004055>
- Zubovich, A. V., Wang, X.-Q., Scherba, Y. G., Schelochkov, G. G., Reillinger, R., Reigber, C., et al. (2010). GPS velocity field of the Tien Shan and surrounding regions. *Tectonics*, *29*, TC6014. <https://doi.org/10.1029/2010TC002772>

Reference From the Supporting Information

- Carlson, W. D., Donelick, R. A., & Ketcham, R. A. (1999). Variability of apatite fission-track annealing kinetics: I. experimental results. *American Mineralogist*, *84*, 1213–1223.
- Hurfurd, A. J., & Green, P. F. (1982). A user's guide to fission track dating calibration. *Earth and Planetary Science Letters*, *50*, 343–354.
- Hurfurd, A. J., & Green, P. F. (1983). The zeta age calibration of fission track dating. *Isotope Geoscience*, *1*, 285–317.
- Jonckheere, R., Enkelmann, E., Min, M., Trautmann, C., & Ratschbacher, L. (2007). Confined fission tracks in ion-irradiated and step-etched prismatic sections of Durango apatite. *Chemical Geology*, *242*, 202–217. <https://doi.org/10.1016/j.chemgeo.2007.03.015>
- Jonckheere, R., Ratschbacher, L., & Wagner, G. A. (2003). A repositioning technique for counting induced fission-tracks in muscovite external detectors in single-grain dating of minerals with low and inhomogeneous uranium concentrations. *Radiation Measurements*, *37*, 217–219. [https://doi.org/10.1016/s1350-4487\(03\)00029-5](https://doi.org/10.1016/s1350-4487(03)00029-5)
- Ketcham, R. A., Donelick, R. A., & Carlson, W. D. (1999). Variability of apatite fission-track annealing kinetics: III. Extrapolation to geological time scales. *American Mineralogist*, *84*, 1235–1255.
- Min, M., Enkelmann, E., Jonckheere, R., Trautmann, C., & Ratschbacher, L. (2007). Measurements of fossil confined fission tracks in ion-irradiated apatite samples with low track densities. *Nuclear Instruments and Methods in Physics Research B*, *259*, 943–950. <https://doi.org/10.1016/j.nimb.2007.03.012>
- Reiners, P. W., & Nicolescu, S. (2006). Measurement of parent nuclides for (U-Th)/He chronometry by solution sector ICP-MS, ARHDL Report 1, www.geo.arizona.edu/~reiners/arhdl/arhdl.htm.
- Sperner, B., Jonckheere, R., & Pfänder, J. A. (2014). Testing the influence of high-voltage mineral liberation on grain size, shape and yield, and on fission track and ⁴⁰Ar/³⁹Ar dating. *Chemical Geology*, *371*, 83–95. <https://doi.org/10.1016/j.chemgeo.2014.02.003>
- Vermeech, P. (2012). On the visualization of detrital age distributions. *Chemical Geology*, *312–313*, 190–194. <https://doi.org/10.1016/j.chemgeo.2012.04.021>

Erratum

In the originally published version of this article, a typesetting error resulted in panels e-g not publishing with Figure 3. The figure has since been corrected, and this version may be considered the authoritative version of record.